MATERIALS SCIENCE

Photocatalytic manipulation of Ca^{2+} signaling for regulating cellular and animal behaviors via MOF-enabled H_2O_2 generation

Zherui Zhang[1]†, Yuhao Luo[2]†, Yuanhong Ma[1], Yaofeng Zhou[3], Dingcheng Zhu[1]*, Wanhua Shen[2]*, Junqiu Liu[1]*

The in situ generation of H_2O_2 in cells in response to external stimulation has exceptional advantages in modulating intracellular Ca^{2+} dynamics, including high controllability and biological safety, but has been rarely explored. Here, we develop photocatalyst-based metal-organic frameworks (DCSA-MOFs) to modulate Ca^{2+} responses in cells, multicellular spheroids, and organs. By virtue of the efficient photocatalytic oxygen reduction to H_2O_2 without sacrificial agents, photoexcited DCSA-MOFs can rapidly trigger Ca^{2+} outflow from the endoplasmic reticulum with single-cell precision in a repeatable and controllable manner, enabling the propagation of intercellular Ca^{2+} waves (ICW) over long distances in two-dimensional and three-dimensional cell cultures. After photoexcitation, ICWs induced by DCSA-MOFs can activate neural activities in the optical tectum of tadpoles and thighs of spinal frogs, eliciting the corresponding motor behaviors. Our study offers a versatile optical nongenetic modulation technique that enables remote, repeatable, and controlled manipulation of cellular and animal behaviors.

INTRODUCTION

The capacity of calcium (Ca^{2+}) signaling to activate downstream effector proteins enables it to regulate diverse cellular physiological processes (*1*). Manipulating cell Ca^{2+} dynamics can directly control cellular proliferation (*2*), differentiation (*3*), gene expression (*4*), and secretion (*5*), as well as treat Ca^{2+} dysregulation–related diseases (*6*). Encouragingly, a variety of external energy field–responsive nanomaterials and nanodevices have been implanted in target cells or tissues for remote, repeatable, and controlled activation of cellular Ca^{2+} signaling and corresponding animal behaviors (*7*–*10*). As the largest Ca^{2+} store in eukaryotic cells, endoplasmic reticulum (ER) stimulation is an infrequently used but effective strategy for remotely regulating cytosolic Ca^{2+} (*11*). This strategy activates Ca^{2+} channels on the ER membrane directly while minimizing interference with other organelles. Of these Ca^{2+} channels, the ubiquitously expressed inositol 1,4,5-trisphosphate receptors (IP_3Rs) can mediate Ca^{2+} signaling through the Ca^{2+} release from ER (*12*). The IP_3R_1 isoform contains 60 cysteine residues, 55 of which are susceptible to oxidation by reactive oxygen species (ROS) (*13*). Therefore, IP_3Rs serve as the potential targets for ROS-mediated thiol oxidation and Ca^{2+} release (*14*). Among the diverse types of ROS, hydrogen peroxide (H_2O_2) is the most desirable activator due to its long lifetime and diffusion distance, as well as its relatively low toxicity (*15*).

Relevant strategies for the introduction of H_2O_2 into target tissue primarily involve the exogenous H_2O_2 delivery (*16*) or in situ H_2O_2 generation [e.g., glucose oxidase–carrying drug delivery vehicles (*17*) and metal peroxide nanoparticles (*18*)]. Nonetheless, these methods with poor controllability pose safety concerns due to premature H_2O_2 leakage or "always-on" H_2O_2 production. On-demand generation of H_2O_2 within localized regions of cells in response to light would alleviate the adverse effect and permit precise regulation of intracellular Ca^{2+} dynamics. Emerging metal-free semiconductor photocatalysts capable of nonsacrificial H_2O_2 photosynthesis (*19*) hold great potential for biological applications owing to a lack of reliance on toxic organic sacrificial reagents and controllable H_2O_2 generation. Hydrophobic small-molecule photocatalysts (*20, 21*), whose photoelectrical properties and functionality can be precisely and flexibly tailored via molecular structure design, are more advantageous in integrating into delivery vehicles. The carrier-mediated payload of small-molecule photocatalysts is a promising photocatalytic cellular Ca^{2+} modulation strategy that offers high loading efficiency without impeding the mass transfer of reactants and products. Constructing metal-organic frameworks (MOFs) by coordinating photocatalysts as organic linkers to metal ions/clusters can densely pack photocatalysts for high loading content and improve their water dispersity while avoiding the photochemical deactivation caused by intermolecular interactions (i.e., aggregation-caused quenching effect), thereby preserving their high photocatalytic properties (*22, 23*).

Here, we constructed an intracellular Ca^{2+} store regulating system with MOFs assembled from the small-molecule photocatalyst, which efficiently generated H_2O_2 under visible light in cells to activate IP_3Rs and liberate Ca^{2+} from ER. As shown in Fig. 1A, 13 small molecules with distinct aromatic structures and substituents are designed, and their H_2O_2 production efficiencies are evaluated. 9,10-Di(p-carboxystyryl)anthracene (DCSA), the derivative of the lead photocatalyst **IIIc**, coordinates to the Zr_6 cluster to form MOFs (DCSA-MOFs) with high loading content and excellent water dispersion (Fig. 1B). DCSA-MOFs are endocytosed into cells or associated with the neuronal plasma membrane. Upon visible light irradiation, H_2O_2 is locally photosynthesized via an oxygen reduction reaction (ORR) and rapidly activates IP_3Rs for thiol oxidation, thereby allowing Ca^{2+} to flow out of ER without damaging cells (Fig. 1C). Activation of Ca^{2+} response in a single cell further leads to the propagation of intercellular Ca^{2+} waves (ICWs) in two-dimensional (2D) and 3D cell (co-)cultures. In addition, this system

[1]College of Material, Chemistry, and Chemical Engineering, Key Laboratory of Organosilicon Chemistry and Material Technology, Ministry of Education, Hangzhou Normal University, Hangzhou 311121, China. [2]Zhejiang Key Laboratory of Organ Development and Regeneration, College of Life and Environmental Sciences, Hangzhou Normal University, Hangzhou, Zhejiang 310036, China. [3]Westlake University, Shilongshan Rd. Cloud Town, Xihu District, Hangzhou, Zhejiang, China. *Corresponding author. Email: shen@hznu.edu.cn (W.S.); zhudc@hznu.edu.cn (D.Z.); junqiuliu@hznu.edu.cn (J.L.)
†These authors contributed equally to this work.

enables remote photoactivation of neurons in the optical tectum of tadpoles and thighs of spinal frogs to elicit corresponding behavioral responses (Fig. 1D). This is the first system reported to use H_2O_2 as the trigger to controllably modulate intracellular Ca^{2+} dynamics by releasing endogenous Ca^{2+} in diverse cell types, through activating ubiquitously expressed IP_3Rs with nanoparticles designed for visible light–triggered H_2O_2 generation.

RESULTS

Syntheses of small-molecule photocatalysts and evaluation of photocatalytic capacity

To in situ photosynthesize H_2O_2 for modulating Ca^{2+} response, 13 small-molecule photocatalysts were designed by substituting benzene (**Ia**), naphthalene (**IIa** and **IIb**), anthracene (**IIIa**-**IIIf**), naphthacene (**IVa** and **IVb**), and pentacene (**Va** and **Vb**) with ethynyl,

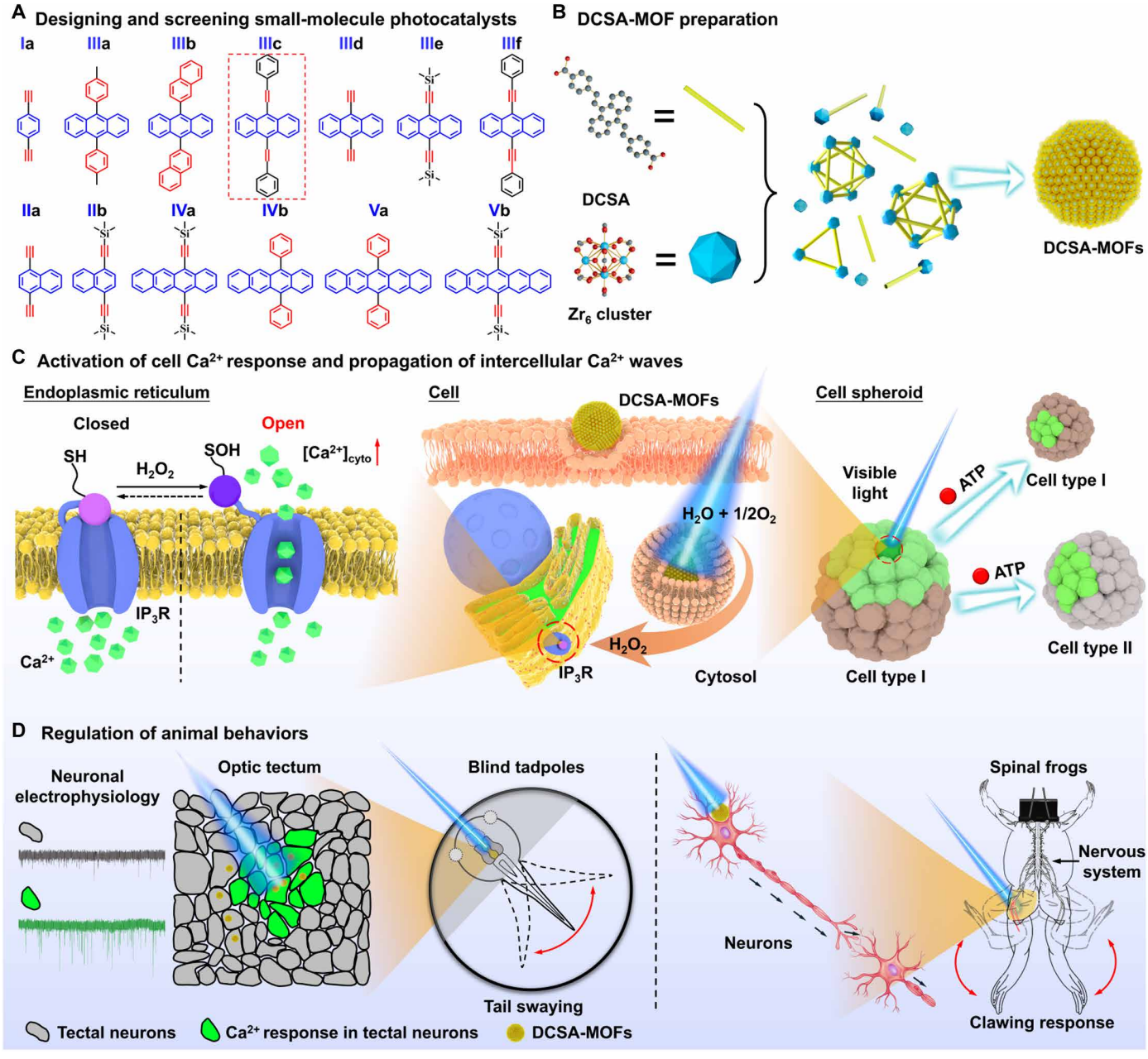

Fig. 1. Schematic illustration of intracellular Ca^{2+} store modulation by H_2O_2 to elicit cell Ca^{2+} response. (**A**) Thirteen small-molecule organic photocatalysts are designed, and the lead compound **IIIc** with the highest photocatalytic activity is screened out. (**B**) The **IIIc** derivative, i.e., 9,10-di(p-carboxystyryl)anthracene (DCSA), coordinates to Zr_6 clusters to construct DCSA-MOFs with high DCSA loading content and excellent aqueous dispersion. (**C**) Photoexcited cell Ca^{2+} response and propagation of intercellular Ca^{2+} waves. Photoexcitation of DCSA-MOFs rapidly generates H_2O_2 from H_2O and O_2, which oxidizes thiol groups of overexpressed IP_3Rs in the endoplasmic reticulum (ER) of targeted cells to efficiently release Ca^{2+} with subcellular precision. The stimulated cell further secretes extracellular ATP to propagate Ca^{2+} waves in 3D cell (co-)cultures. IP_3Rs, inositol 1,4,5-trisphosphate receptors; -SOH, sulfenic acid; -SH, thiol group. (**D**) Photoactivation of neurons and manipulation of animal behaviors. After local microinjection of DCSA-MOFs, photoexcitation activates tectal neurons and causes tail swaying in blind tadpoles and clawing responses in spinal frogs.

(trimethylsilyl)ethynyl, phenyl, naphthyl, styryl, and phenyl ethynyl groups (Fig. 1). The detailed synthetic procedure is described in section S1. The intermediate and final products were identified by nuclear magnetic resonance (NMR) spectra (figs. S2 to S27). The anthracene derivative **IIId** and deprotected product of naphthacene derivative **IVa** containing highly reactive alkynyl hydrogen (-C ≡ CH) were quite unstable, probably attributed to the polymerization of alkynyl hydrogen into insoluble branched polymers (*24*). Even with the trimethylsilyl protecting group, pentacene derivative **Vb** was extremely unstable at ambient conditions, let alone its deprotected product.

Next, we evaluated the photocatalytic activity of 13 structures. Photocatalysts were dissolved in chloroform, and water as the reactant was added to collect the produced H_2O_2 (fig. S44). Given the different absorbance of photocatalysts (fig. S43, A to M), the reaction system was illuminated under simulated AM 1.5 G solar light by a xenon arc lamp (0.68 W/cm^2), whose spectral radiant intensity was nearly homogeneous ranging from 350 nm to 780 nm (fig. S43N). As shown in Fig. 2A, the substitution of the alkynyl hydrogen with trimethylsilyl (**IIa** versus **IIb,** and **IIId** versus **IIIe**) or phenyl (**IIId** versus **IIIf**) groups compromised H_2O_2 photosynthesis. The top three structures (**IIIc**, **IIId**, and **IIIa**) were all anthracene derivatives. Within 3 hours of illumination, the lead compound **IIIc** achieved an H_2O_2 evolution rate of 405.2 ± 22.7 μmol H_2O_2/mmol photocatalyst per hour, which was 1.3 and 2.4 times more efficient than **IIId** and **IIIa**, respectively. The controllability of photocatalytic H_2O_2 production of **IIIc** was assessed by cycling the illumination on and off six times every 30 min. H_2O_2 production followed a pulsatile profile: the H_2O_2 concentration increased notably during illumination and remained almost constant in the dark (Fig. 2B). Collectively, **IIIc** had superior advantages over others, including facile synthesis and functionalization, high stability, exceptional photocatalytic performance, and on-demand H_2O_2 generation. Consequently, it was chosen for further investigations.

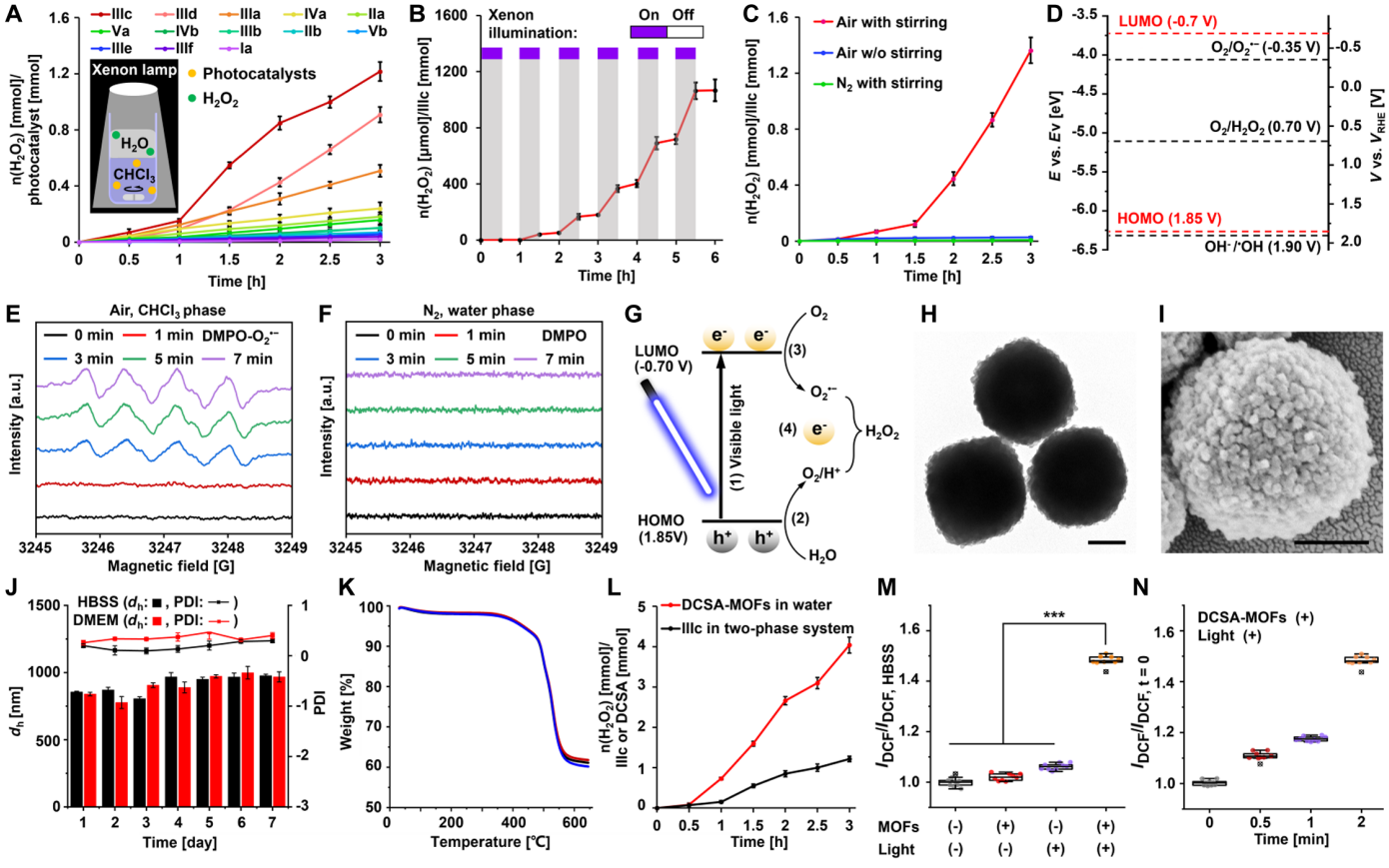

Fig. 2. Preparation and characterizations of the photocatalyst IIIc and the resulting DCSA-MOFs. (**A**) H_2O_2 evolution rate of 13 small-molecule photocatalysts in a biphasic system illuminated by a xenon arc lamp. (**B**) On-demand H_2O_2 generation of **IIIc** after exposure to six 30-min on/180-min off light cycles. (**C**) H_2O_2 generation of **IIIc** in the air with or without agitation, or in the N_2 atmosphere with agitation. (**D**) Band structure diagram of the HOMO/LUMO energy level of **IIIc** (red lines) with respect to $O_2/O_2^{\bullet-}$, O_2/H_2O_2, and $OH^-/^{\bullet}OH$ reduction potentials. (**E** and **F**) DMPO spin-trapping ESR spectra recorded for $O_2^{\bullet-}$ and $^{\bullet}OH$ in chloroform or water phase with **IIIc** and xenon illumination in the air or N_2 atmosphere. (**G**) Schematic illustration of H_2O_2 photosynthesis via ORR pathway. (**H**) SEM and (**I**) TEM images showing the morphology of DCSA-MOFs. Scale bar, 200 nm. (**J**) Mean hydrodynamic diameter (d_h) of DCSA-MOFs in cell culture medium containing 10% FBS or HBSS over 7 days ($n = 3$ per group). (**K**) Three measurements of thermogravimetric curves of DCSA-MOFs in the N_2 atmosphere. (**L**) Photocatalytic H_2O_2 generation of DCSA-MOFs and **IIIc** illuminated by a xenon arc lamp. (**M**) DCF fluorescent intensity (I_{DCF}) after 2 min of treatment under different conditions ($n = 9$ per group). (**N**) Time-dependent increase in I_{DCF} after 0 to 2 min of illumination on DCSA-MOF solution ($n = 9$ per group). For the box plot, the center line represents the mean value. The bottom and upper edges of the box represent the 25th and 75th percentiles, respectively. Whiskers extending to extreme data points were not considered outliers (marked with a cross). Significances are determined by one-way analysis of variance (ANOVA) with Tukey's correction. ***$P < 0.001$.

Photocatalysts are known to produce H_2O_2 through the ORR pathway, which reduces O_2 to $O_2^{\bullet-}$ or water oxidation reaction (WOR), which oxidizes H_2O to $^{\bullet}OH$, or both (*19*). Figure 2C indicates the involvement of the ORR pathway, as the lack of O_2 completely ceased H_2O_2 generation. The cyclic voltammetry data show that the lowest unoccupied molecular orbital (LUMO) potential of **IIIc** was −0.70 V versus reversible hydrogen electrode (RHE; Fig. 2D, fig. S46, and table S1), which was more negative than the potential of $O_2/O_2^{\bullet-}$ reduction (−0.35 V versus RHE). Thermodynamically, the photoexcited electrons from the LUMO of **IIIc** can reduce O_2 to $O_2^{\bullet-}$. In contrast, **IIIc** was incapable of oxidizing OH^- to $^{\bullet}OH$ because the reduction potential of $OH^-/^{\bullet}OH$ (1.90 V versus RHE) was more positive than the highest occupied molecular orbital (HOMO) potential of **IIIc** (1.85 V versus RHE). The existence of short-lived $O_2^{\bullet-}$ and $^{\bullet}OH$ in the two-phase system containing **IIIc** was further investigated using electron spin resonance (ESR) spectroscopy with 5,5-dimethyl-1-pyrroline N-oxide (DMPO) as the trapping probe in the aerobic or anaerobic condition. In the chloroform phase, the characteristic signal peaks of DMPO-$O_2^{\bullet-}$ adduct confirmed rapid production of $O_2^{\bullet-}$ in the air (Fig. 2E), but not in anaerobic conditions (fig. S47A). In anaerobic conditions, the characteristic signal peaks of DMPO-$^{\bullet}OH$ cannot be observed in the water phase (Fig. 2F), confirming that **IIIc**-excited holes cannot oxidize OH^- to $^{\bullet}OH$. Nonetheless, we observed evident DMPO-$^{\bullet}OH$ signals in the water phase in the air (fig. S47B), most likely due to H_2O_2 photolysis into $^{\bullet}OH$ (*25*). Hence, we inferred that photocatalytic H_2O_2 generation over **IIIc** involves the following four reactions (*26, 27*) (Fig. 2G):

$$\text{DCSA} + \text{visible light} \rightarrow h^+ + e^- \quad (1)$$

$$2h^+ + H_2O \rightarrow (1/2)O_2 + 2H^+ \quad (2)$$

$$e^- + O_2 \rightarrow O_2^{\bullet-} \quad (3)$$

$$e^- + O_2^{\bullet-} + 2H^+ \rightarrow H_2O_2 \quad (4)$$

To understand the catalytic mechanism of H_2O_2 production, we performed the density functional theory (DFT) calculations with model systems of **Ia** to **Vb**. The process of ORR-mediated H_2O_2 photosynthesis commences with adsorption of O_2 as the substrate onto the active sites of catalysts. Subsequently, H_2O_2 is generated through the activation and hydrogenation of O_2, a process that encompasses the formation of various intermediates and transition states (TSs) (*28, 29*). Therefore, it is crucial to consider both the O_2 adsorption and activation processes of a molecule to evaluate the photocatalytic activity (*30, 31*). A high O_2 adsorption energy (E_{ads}) indicates a strong affinity for O_2 adsorption, which is the fundamental requirement for achieving high catalytic activity. As anticipated, **IIIc** has the highest E_{ads} among 13 molecules (fig. S105). Other factors that affect E_{ads} include the following: (i) The presence of trimethylsilyl (TMS) group hinders the process of O_2 adsorption (**IIa** versus **IIb**: −1.0 kcal/mol versus −0.3 kcal/mol; **IIId** versus **IIIe**: −3.3 kcal/mol versus −0.3 kcal/mol). (ii) Molecules comprising anthracene (**IIIa** to **IIIf**), with the exception of **IIIe** (with TMS group), exhibit greater E_{ads} than those containing benzene (**Ia**), naphthalene (**IIa**, **IIb**), naphthacene (**IVa**, **IVb**), and pentacene (**Va**, **Vb**). The order of increase for the top five photocatalysts with the highest E_{ads} is as follows: **IIIc** > **IIId** > **IIIa** >> **IIIf** > **IIIb**.

Then, the proposed reaction mechanisms of the ORR pathways for each of those five photocatalysts were figured out (fig. S106), along with a comparison of their respective energy barriers of TSs during the O_2 activation process (fig. S107). The lower activation energy, the higher reaction rate. Throughout the entire H_2O_2 production process, TS energy barriers required by intermediate species OOH* and HOOH* increased in the order of **IIIc** < (**IIId**, **IIIa**) << (**IIIb**, **IIIf**), indicating that **IIIc** catalyzes at a faster reaction rate than the others. Collectively, fig. S108 illustrates the correlation among the E_{ads}, energy barriers of TSs, and photocatalytic H_2O_2 activity. A photocatalyst that has a high affinity for adsorbing O_2 and TSs with low free energies is anticipated to demonstrate exceptional photocatalytic activity.

Preparation and characterizations of DCSA-MOFs

For intracellular delivery, we first encapsulated **IIIc** into a liposome, which consisted of lecithin and cholesterol at a mass ratio of 10:1. However, the loading content and encapsulation efficiency were only 0.46 ± 0.02% and 10.1 ± 0.5%, respectively, probably due to the crystallization tendency induced by the strong π-π interaction between planar polycyclic aromatic structures. To increase the loading capacity of **IIIc** for high Ca^{2+} modulation efficiency, MOFs were assembled through the robust coordination interaction between the carboxylic group of its derivative DCSA (syntheses and characterizations were shown in figs. S28 to S36) and the Zr_6 cluster. The characteristic absorption peaks of **IIIc**, DCSA, and DCSA-MOFs were 411, 414, and 429 nm, respectively (fig. S38A). Their emission peaks were 663, 627, and 595 nm, respectively (fig. S39B). DCSA also exhibited comparable HOMO/LUMO level to that of **IIIc** (fig. S46 and table S1). The transmission electron microscope (TEM) and scanning electron microscope (SEM) images exhibit polyhedral nanoparticles with a rough surface deposited with multiple smaller nanoparticles (Fig. 2, H and I, and fig. S37). The type II isotherms of N_2 sorption show that DCSA-MOFs were nonporous materials with Brunauer-Emmett-Teller (BET) surface area of 19.4 m^2/g (fig. S39). DCSA-MOFs had a hydrodynamic size of 863.3 ± 26.4 nm [polydispersity index: 0.20 ± 0.04, as determined by dynamic light scattering (DLS); fig. S40A] and a ζ potential of −11.5 ± 0.2 mV (fig. S40B). Moreover, DLS results proved high stability of DCSA-MOFs in Hanks' balanced salt solution (HBSS), cell culture medium containing 10% fetal bovine serum (FBS) (Fig. 2J), and acidic acetic acid/sodium acetate (HAc-NaAc) buffer (10 mM, pH 5.0) (fig. S41) over 1 week. DCSA-MOFs maintained their morphological integrity without damage or erosion after 7 days in HAc-NaAc buffer (fig. S42). These properties are advantageous for long-term manipulation within biological systems.

According to the thermogravimetric analysis (TGA) curve (Fig. 2K), the loading content and encapsulation efficiency of DCSA were 46.9 ± 0.7% and 31.1 ± 0.5%, respectively. The high connectivity on the Zr_6 cluster inside DCSA-MOFs led to a substantial improvement in the loading capacity of DCSA, hence resulting in a substantial reduction in carrier dose. DCSA-MOFs dispersed in water produced H_2O_2 3.3 times more than that of **IIIc** in the biphasic system (Fig. 2L). The enhanced catalytic activity can be ascribed to the rough surface. The presence of numerous tiny nanoparticles onto DCSA-MOFs dramatically increased surface area to volume ratio by about 17.3 times (estimation was referred to in section S2.5) compared to a smooth nonporous sphere

of the same size, which dramatically increased the contact area between the reactants and DCSA molecules.

Short-term H_2O_2 production was further detected by monitoring the fluorescence intensity of 2′,7′-dichlorodihydrofluorescein (H_2DCFH), as H_2O_2 could oxidize nonfluorescent H_2DCFH to fluorescent 2′,7′-dichlorofluorescein (DCF). The sharp increment in DCF fluorescence intensity (denote I_{DCF}) required the coexistence of DCSA-MOFs and illumination. In contrast, control groups lacking either DCSA-MOFs or illumination exhibited minimal changes (Fig. 2M). The H_2O_2 evolution rate showed a positive correlation with the duration of irradiation, reaching approximately 1.5 times the I_{DCF} after 2 min (Fig. 2N).

DCSA-MOFs triggered Ca^{2+} response in a single cell

After demonstrating the excellent photocatalytic capacity of DCSA-MOFs in generating H_2O_2, their potential cytotoxicity against mouse cardiomyocyte HL-1 cells was assessed using the cholecystokinin octapeptide assay. More than 90% viability was maintained after 24 or 48 hours of exposure to DCSA-MOFs (10 μg/ml) (fig. S50), indicating no acute toxicity under the experimental conditions. To explore the endocytic pathways through which DCSA-MOFs entered cells, cells were co-incubated with DCSA-MOFs and specific chemical endocytic inhibitors at nontoxic concentrations. Flow cytometry was used to quantify cellular uptake based on the fluorescence intensity of DCSA-MOFs. Figure S51 shows that the uptake ratio decreased dramatically to approximately 27.3% at 4°C, indicating that this process was energy dependent. The internalization was affected to comparable degrees by chlorpromazine (an inhibitor of clathrin-mediated endocytosis, uptake ratio: about 41.6%), genistein (an inhibitor of caveolae-mediated endocytosis, approximately 48.8%), and wortmannin (an inhibitor for macropinocytosis, about 50.3%). Cytochalasin D, which inhibited actin polymerization, only slightly reduced the uptake to about 72.2%. Hence, DCSA-MOFs entered cells via multiple pathways.

H_2O_2 as a second messenger is known to elevate $[Ca^{2+}]_{cyto}$ in numerous cell types at concentrations of 0.5 to 10 mM (*32, 33*). Figure S66 shows that the threshold concentration of H_2O_2 that could stimulate HL-1 cells was 1 mM, which induced a delayed increase in $[Ca^{2+}]_{cyto}$ compared to the photoexcited Ca^{2+} response (fig. S65). This was ascribed to slowed diffusion of H_2O_2 across the plasma membranes (*34*). Of note, H_2O_2 hardly affected $I_{Fluo\text{-}8}$ (fig. S55, B and D). Using the ROS indicator H_2DCFH, the elevation in intracellular ROS levels after illumination was measured. As depicted in Fig. 3A, I_{DCF} of HL-1 cells with endocytosed DCSA-MOFs increased approximately four times compared to the control without DCSA-MOFs after 2 min of xenon illumination. Upon photoexcitation of DCSA-MOFs (as indicated by the red box) by a 488-nm laser (20× objective, CLSM900) with a laser power P_{laser} = 2.27 mW for 0.16 s, the I_{DCF} of the irradiated cell first rapidly increased to 1.2 to 1.3 times its initial value and then either increased continuously (Fig. 3B) or remained constant (fig. S68). However, the intracellular ROS levels of cells photoexcited in blank regions (represented by other colored boxes) remained unchanged. Therefore, only photoexcitation of DCSA-MOFs could efficiently and rapidly elevate the intracellular ROS levels, and locally generated H_2O_2 cannot diffuse to other cells.

Subsequently, the ability of DCSA-MOFs to regulate intracellular Ca^{2+} dynamics in response to local photoexcitation was tested in 10 distinct cell lines, including human breast cancer MCF-7 cell, cervical cancer HeLa cell, malignant glioma U87MG cell, lung adenocarcinoma A549 cell, murine melanoma B16F10 cell, mammary carcinoma 4T1 cell, rat pheochromocytoma PC-12 undifferentiated cell, mouse embryonic fibroblast NIH-3T3 cell, HL-1 cell, and isolated primary astrocyte. Cells were incubated with DCSA-MOFs (10 μg/ml) for 24 hours and loaded with the Ca^{2+} indicator Fluo-8. Confocal laser scanning microscope (CLSM) enabled simultaneous photoexcitation in a custom-defined region and real-time monitoring of Fluo-8 fluorescence intensity (abbreviated as $I_{Fluo\text{-}8}$) (*35, 36*). Of note, the emission spectrum of DCSA-MOFs ranged from 500 to 900 nm (fig. S38B) and partially overlapped that of Fluo-8 (fig. S55A). This fluorescence cross-talk made DCSA-MOFs also visible as punctate signals in the Fluo-8 fluorescence channel, while Fluo-8 was uniformly distributed throughout the whole cells. Irradiation at 488 nm with a laser power P_{laser} = 2.27 mW for 0.16 s on the region without DCSA-MOFs (as indicated by a blue box in Fig. 3C) could not trigger a Ca^{2+} response. When cells were not loaded with Fluo-8, laser irradiation on DCSA-MOFs was also unable to increase $I_{Fluo\text{-}8}$ (fig. S57), hence excluding the possibility that the fluorescence originated from DCSA-MOFs. In contrast, photoexcitation of DCSA-MOFs (as indicated by a red box in Fig. 3C) instantly triggered a Ca^{2+} response in a single HL-1 cell (movie S1) and other cell lines (fig. S58). Despite the variations in sizes and morphologies among the tested cells, a localized rise in cytosolic Ca^{2+} concentration (denoted $[Ca^{2+}]_{cyto}$) initiated in the irradiated region immediately following irradiation and spread rapidly to other regions within the cell. Because of the Ca^{2+}-induced Ca^{2+} release process (*37*), an intrinsic Ca^{2+} signaling amplification mechanism, the ongoing increase in $I_{Fluo\text{-}8}$ could persist for several minutes before reaching a plateau. After a few minutes, $[Ca^{2+}]_{cyto}$ of a stimulated cell gradually decayed to its baseline (Fig. 3C), in accordance with our previous experimental results (*35*). In contrast to the fast-spiking firing pattern of Ca^{2+} signaling with short durations (<0.5 s) via activating ion channels on the plasma membrane (*38*), our system allowed long-lasting elevation of $[Ca^{2+}]_{cyto}$, thereby reducing the stimulation times and stimulation caused potential cell damage. Additionally, the same cell can be photoexcited repeatedly by sequentially irradiating different DCSA-MOFs (Fig. 3D and fig. S59), demonstrating the potential for sustained regulation of Ca^{2+}-relevant biological processes. Using a 405-nm laser pointer (spot diameter: 1 cm) with a laser power P_{laser} = 1.5 W for 9 s, we could irradiate multiple HL-1 cells simultaneously and observed a great increment in $[Ca^{2+}]_{cyto}$ in nearly all irradiated cells (fig. S60). This finding suggests that DCSA-MOFs were also applicable in other illumination systems.

H_2O_2-triggered Ca^{2+} release from ER

Numerous studies have been conducted to investigate the mechanism underlying H_2O_2-induced Ca^{2+} signaling; however, the mechanisms remain inconclusive. To determine the source of Ca^{2+}, i.e., exogenous Ca^{2+} in the culture medium or endogenous Ca^{2+} in the intracellular Ca^{2+} stores, photoexcitation was performed in the culture medium ($[Ca^{2+}]$: 1.8 mM), Ca^{2+}-containing HBSS ($[Ca^{2+}]$: 1.26 mM), and Ca^{2+}-free HBSS ($[Ca^{2+}]$: 0 mM). Similar Ca^{2+} responses were observed (fig. S69), ruling out the possibility of Ca^{2+} influx through either the plasma membrane cation channels or disrupted pores in the plasma membrane. Confocal images displayed more than 70% of DCSA-MOFs (shown in green) colocalized with

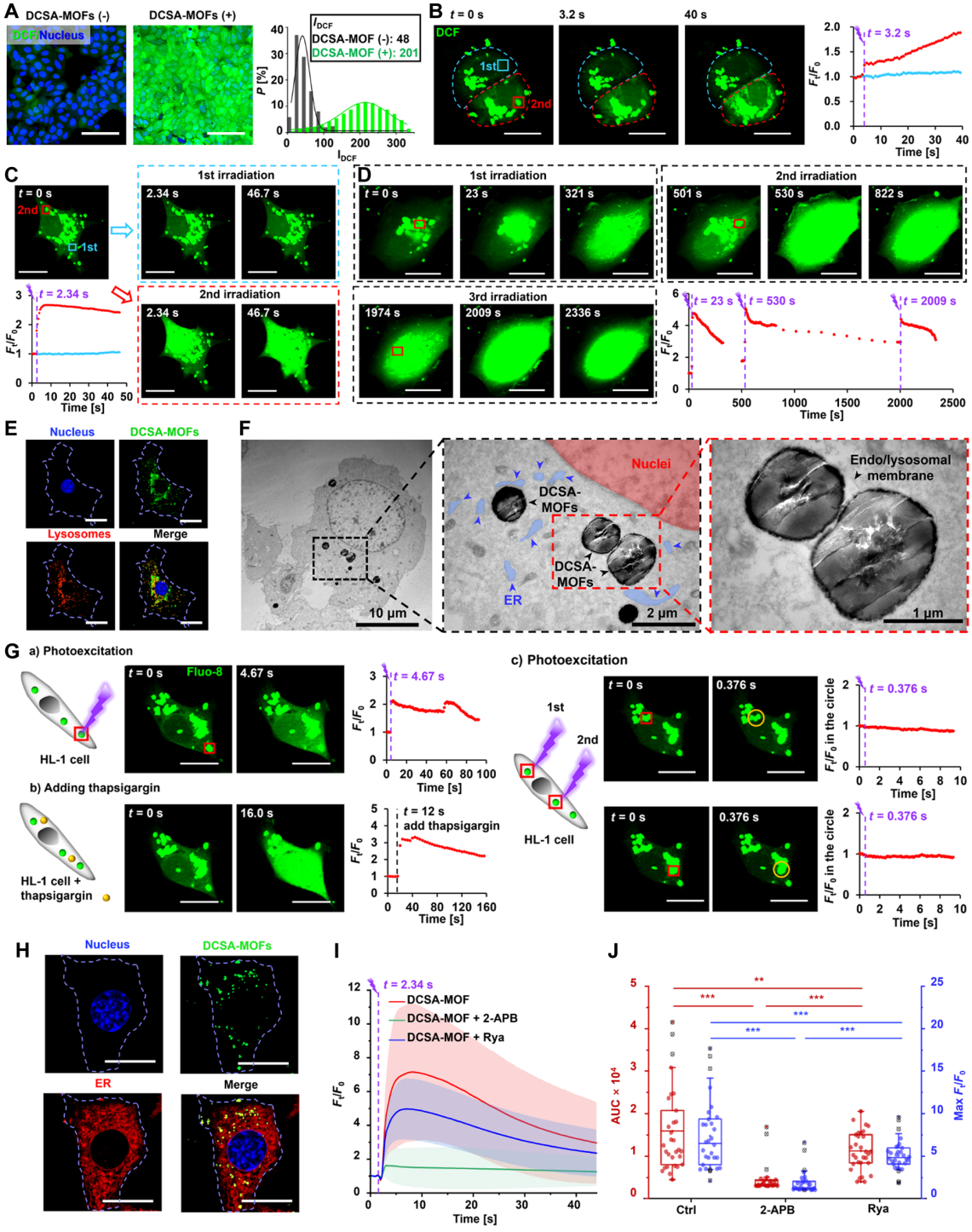

Fig. 3. H_2O_2-evoked Ca^{2+} response in photoexcited HL-1 cells and the underlying mechanism. (**A** and **B**) Photoexcitation of DCSA-MOFs elevated intracellular ROS levels. HL-1 cells were photoexcited by (A) a xenon light (0.68 W/cm^2) for 120 s or (B) the 488-nm CLSM laser (2.27 mW) for 0.16 s. Intracellular ROS levels in terms of DCF fluorescence intensity (I_{DCF}) were quantified from the images. (**C**) Photoexcitation of DCSA-MOFs increased $[Ca^{2+}]_{cyto}$ in an isolated HL-1 cell by the 488-nm CLSM laser. (**D**) Repetitive stimulation of an isolated HL-1 cell. (**E**) Colocalization of DCSA-MOFs (green) and lysosomes (red). The nucleus stained with Hoechst 33342 is shown in blue. Plasma membrane stained with wheat germ agglutinin–Alexa Fluor 633 is shown in gray, and its boundary is indicated by a dashed blue line. (**F**) TEM images of HL-1 cells after incubation with DCSA-MOFs for 48 hours. Black arrows indicated DCSA-MOFs. Blue arrows indicated ER. (**G**) Photoexcitation released Ca^{2+} did not originate from lysosomes. (a) DCSA-MOFs indicated by the red box were irradiated by the 488-nm CLSM laser. (b) Thapsigargin (500 nM) in Ca^{2+}-free HBSS was added to the cells. (c) Once $[Ca^{2+}]_{cyto}$ was restored to the baseline, other DCSA-MOFs were irradiated. (**H**) Intracellular distributions of DCSA-MOFs and ER. ER stained with ER–Tracker Red is shown in red. (**I**) Ca^{2+} response curves of HL-1 cells pretreated with 200 μM 2-APB or 25 μM Rya. The solid line represents the average value. Shading represents the SD ($n = 30$ per group). (**J**) Area under the curve (AUC) and peak values calculated from (H). $^{**}P < 0.01$; $^{***}P < 0.001$. Scale bars, 100 μm in (A) and 20 μm in others.

lysosomes (red) as yellow dots after 12 and 24 hours of incubation (Fig. 3E and fig. S52), indicating that most DCSA-MOFs were trafficked to lysosomes after endocytosis. TEM results further validated that DCSA-MOFs were wrapped in the endo/lysosomal membrane after 24 or 48 hours of incubation (Fig. 3F and fig. S54), and their structural integrity remained unaltered without erosion. It is known that lysosomal Ca^{2+} leakage can evoke robust Ca^{2+} release from the ER (*35*). Therefore, in the subsequent experiment, several manipulations were performed on the same cell: (i) First, photoexcitation increased $[Ca^{2+}]_{cyto}$ in Ca^{2+}-free HBSS (Fig. 3Ga and fig. S70A), followed by (ii) depletion of ER Ca^{2+} stores by adding thapsigargin (Fig. 3Gb and fig. S70B), a sarco/endoplasmic reticulum Ca^{2+} adenosine triphosphatase (ATPase) (SERCA) inhibitor preventing Ca^{2+} reuptake to the ER, and finally (iii) photoexcitation again on other regions containing DCSA-MOFs (Fig. 3Gc and fig. S70C). In contrast to our previous findings, there was no transient increase in $I_{Fluo\text{-}8}$ around the lysosomes, proving no lysosomal Ca^{2+} release.

Figure 3 (F and H) shows that the endocytosed DCSA-MOFs were surrounded by a densely packed ER network. Therefore, we hypothesized that photo-generated H_2O_2 could diffuse out and activate adjacent IP_3Rs or ryanodine receptors (RyRs) on the ER to induce Ca^{2+} outflow. Before photoexcitation, cells were pretreated with 2-aminoethyl diphenylborane (2-APB) and ryanodine (Rya), specific inhibitors for IP_3Rs and RyRs, respectively. The extent of inhibition in terms of the reduction in area under the curve (AUC) and peak values relative to the control was calculated. Blockade of IP_3Rs decreased the AUC and peak values by 72.2% and 74.7%, respectively, substantially greater than the inhibition of RyRs (reduction in AUC: 29.3% and peak: 31.0%) (Fig. 3, I and J). Collectively, these findings reveal that the locally produced H_2O_2 in the photoexcited cell primarily activated IP_3Rs of nearby ER and triggered their Ca^{2+} release; the locally released Ca^{2+} diffused to other ERs in the same cell and further activated IP_3Rs to elicit a robust Ca^{2+} response via the Ca^{2+}-induced Ca^{2+} release effect.

Propagation of ICWs in 2D cell (co-)cultures

After demonstrating the capability to elicit Ca^{2+} response at the single-cell level, we assessed the propagation of ICWs, which allow cell-to-cell communications in response to external stimuli. After photoexcitation of a single cell, $[Ca^{2+}]_{cyto}$ in adjacent cells was monitored. On the basis of the occurrence probabilities of ICWs, cells can be roughly classified into three categories: (i) NIH-3T3, U87MG, B16F10, and PC-12 cells cannot spread the ICWs (fig. S71); (ii) MCF-7, 4T1, and A549 cells have a chance of doing so (fig. S72); and (iii) HL-1 cells and astrocytes could always propagate the ICWs (Fig. 4, A and C, and movie S2). Within a few to tens of seconds of latency, ICWs spread radially from the stimulated HL-1 cell to distal cells. We also cocultured CellTracker Red CMTPX–labeled MCF-7 cells (shown in red in Fig. 4, E and F, and figs. S74 and S75) and unlabeled HL-1 cells. Regardless of which kind of cell was photoexcited, ICWs spread predominantly in HL-1 cells but rarely in MCF-7 cells (movie S3). Even MCF-7 cells positioned between two responding HL-1 cells failed to react or exhibited a weak response.

Stimulated cells can secrete adenosine triphosphate (ATP) as a purinergic receptor agonist to transmit cell-to-cell Ca^{2+} signaling. Adding 1 mM ATP directly to HL-1 cells induced a rapid Ca^{2+} response in all HL-1 cells (fig. S76). Then, ATP secretion was quantified using a chemiluminescence assay (fig. S80). As expected, HL-1 cells with endocytosed DCSA-MOFs secreted notably more ATP (39.9 ± 6.0 pmol/10^6 cells) after 2 min of xenon illumination, in comparison to controls only treated with DCSA-MOFs or xenon light (fig. S81). To further confirm the involvement of ATP in ICWs, photoexcitation was performed in the presence of apyrase (20 U/ml), an ATP hydrolyzing enzyme that catalyzes the conversion of ATP to adenosine monophosphate (AMP) and inorganic phosphate. $I_{Fluo\text{-}8}$ only increased in the photoexcited cell, whereas ICWs completely diminished (Fig. 4B and figs. S82 and S83). On this basis, we inferred that both HL-1 and MCF-7 cells could secrete ATP in response to photoexcitation. HL-1 cells secreted ATP molecules via connexin 43 (Cx43) hemichannels, as evidenced by the disappearance of ICWs after photoexcitation when 200 μM Gap 19, a potent and selective Cx43 blocker, was applied (fig. S84). In 2D interconnected HL-1 cells (fig. S73A) and HL-1/MCF-7 cell cocultures (fig. S75A), the maximal spread distance of ICWs after irradiating an HL-1 cell was 394 and 257 μm, respectively. In a scratch experiment, the propagation of ICWs was restricted to a distance of about 100 μm (figs. S73B and S75B). These results suggested that ATP secreted from the photoexcited cells induced additional ATP release from nearby cells, allowing ICWs to propagate over a longer distance (*39*).

We discovered that the thresholds of ATP concentration to evoke Ca^{2+} responses varied in cell types. Typically, the approximate threshold values for differentiated PC-12, MCF-7, and HL-1 cells were 125, 0.78, and 0.25 μg/ml, respectively (figs. S77 to S79). That is, the threshold of different cell lines decreased as their probability of spreading ICWs increased. The activation of plasma membrane purinergic receptors by ATP to initiate ICWs is widely acknowledged to occur through the following two mechanisms: (i) Ion channel P2X receptors leads to Ca^{2+} influx, and (ii) G protein–coupled metabotropic P2Y receptors activates phospholipase C (PLC), generates IP_3, and releases Ca^{2+} from the ER (*40*). Such a discrepancy in ATP sensitivity was supposed to be determined by the expression levels of purinergic receptors. Compared to differentiated PC-12 cells, HL-1 cells expressed remarkably more P2X receptors but much fewer P2Y receptors at the mRNA transcription level (fig. S85). Upon treatment with 30 μM pyridoxal phosphate-6-azo(benzene-2,4-disulfonic acid) tetrasodium salt, a nonselective purinergic P2 receptor antagonist of P2X1, P2X2, P2X3, P2X4, P2X5, and P2X7, ICW propagation in HL-1 cells ceased or became delayed and weak (fig. S86A). We further incubated cells with 10 μM 5-(3-bromophenyl)-1,3-dihydro-2H-Ben zofuro[3,2-e]-1,4-diazepin-2-one, which selectively blocks P2X4, and again similar results were observed (fig. S86B). These findings suggest that P2X, and particularly P2X4, played a crucial role in ATP-mediated Ca^{2+} signaling. In contrast, ICWs in interconnected astrocytes propagated in a certain direction (Fig. 4C and movie S4). Confluent astrocytes can form gap junctions that permit direct intercellular transfer of IP_3 (*41*), and thus, astrocytes were preincubated for 1 hour with 200 μM carbenoxolone, a highly selective gap junction blocker, before photoexcitation. As anticipated, the long-distance spreading of ICWs (mean distance: 585 μm) was completely blocked, and only the photoexcited cell responded (Fig. 4D and fig. S87).

Propagation of ICWs in 3D cell (co-)cultures

Modulating Ca^{2+} signaling in 3D cell cultures has been rarely reported (*35, 42*). Conventional chemical, electrical, magnetic, and mechanical approaches cannot precisely stimulate a single cell inside a spheroid without disturbing other cells. For this, we photoexcited a single cell in a multicellular spheroid that mimics small

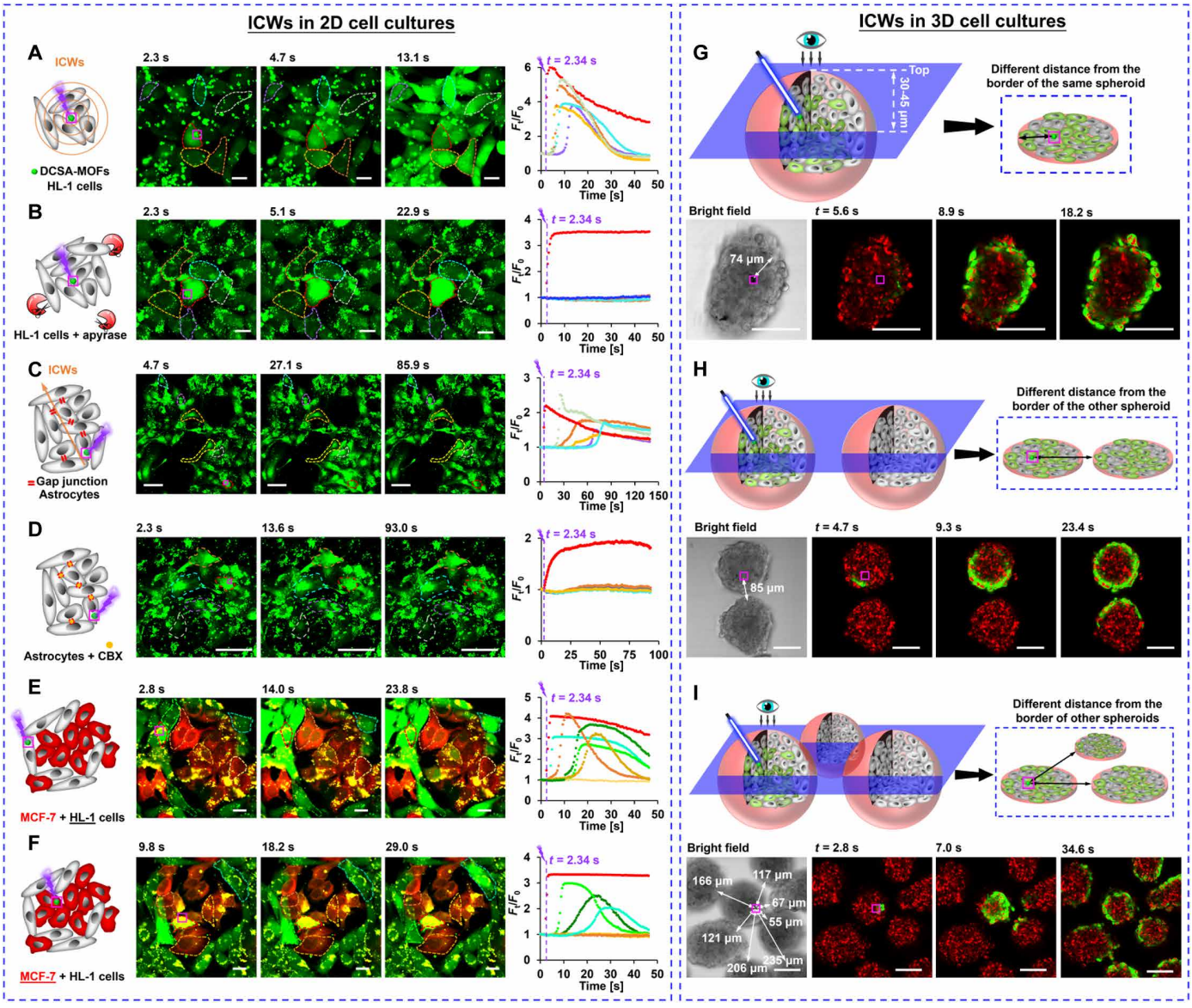

Fig. 4. Propagation of ICWs in 2D and 3D cell (co-)cultures. At time $t = 2.34$ s, endocytosed DCSA-MOFs in the pink box in one cell (indicated by a red dashed line) were irradiated by a 488-nm laser from CLSM at a laser power $P_{laser} = 2.27$ mW for 0.16 s. (**A** to **F**) ICWs spread in 2D (co-)cultures of [(A) and (B)] HL-1 cells, [(C) and (D)] astrocytes, and [(E) and (F)] mixed MCF-7 and HL-1 cells. The curves with different colors indicate the Fluo-8 intensities of cells labeled by corresponding dashed lines. CellTracker Red CMTPX MCF-7 cells were pseudocolored red. [(B) and (D)] Before photoexcitation, cells were preincubated with (B) apyrase (50 U/ml) for 20 min or (D) 200 μM carbenoxolone (CBX) for 1 hour. (**G** to **I**) ICWs spread in 3D cultures of HL-1 cells in (G) one, (H) two, or (I) multiple spheroids. Arrows indicate the distance between irradiated DCSA-MOFs and the edge of (G) the same spheroid or [(H) and (I)] nearby spheroids. Scale bars, 20 μm [(A), (B), (E), and (F)] and 100 μm [(C), (D), and (G) to (I)].

tissues and observed the ICW propagation in one cross-section. Spheroids were formed out of CellTracker Red CMTPX–labeled HL-1 cells (shown in red in Fig. 4, G to I) with endocytosed DCSA-MOFs. Because of the inability of Fluo-8 to stain cells deep inside the spheroids, only superficial cells were observed. Photoexcitation was performed on DCSA-MOFs located at varying distances (2 to 74 μm) from the edge of spheroids, i.e., at the margin or in the center of the spheroids. Ca^{2+} waves were initiated from the photoexcited cell and spread radially inside the spheroid (Fig. 4G and fig. S88). ICWs between two spheroids composed of 200, 600, and 1600 HL-1 cells were then evaluated to mimic inter-tissue communications. For spheroids formed from 600 cells, the distance between the photoexcited DCSA-MOFs in one spheroid and the closest edge of the other one varied between 29 and 238 μm (Fig. 4H and fig. S90). The ratios of responding cells were negatively correlated with the distances: (i) nearly all cells responded at distances less than 55 μm; (ii) the ratios decreased to half or one-third at the distance of between 85 and 150 μm, and those responding cells were closer to the photoexcited position; (iii) there was no Ca^{2+} response in cells located more than 194 μm away from the stimulated cell, indicating that the concentration of diffused ATP was below the responding threshold. The propagation distance of ICWs was found

to be highly correlated with cell density, as spheroids containing 200 and 1600 HL-1 cells exhibited a limit of spread distance of 132 and 235 μm, respectively (figs. S89 to S91). Ca^{2+} waves could also spread as far as 235 μm when numerous spheroids containing 600 cells were mixed (Fig. 4I, fig. S92, and movie S5). Again, these findings demonstrate that ATP secreted from the photoexcited cells triggered the release of ATP from neighboring cells. Therefore, greater ATP production by larger spheroids enabled ICWs to travel a longer distance. We also analyzed the ICWs in mixed HL-1 and MCF-7 spheroids. Like the results in 2D cocultures, ICWs propagated predominantly in HL-1 spheroids but to a much lesser extent in MCF-7 spheroids (figs. S94 and S95).

Activation of tectal neurons for triggering visual avoidance behavior in blind tadpoles

Nanotransducer-enabled wireless regulation of neuronal $[Ca^{2+}]_{cyto}$ has evolved into an effective technique for precise neuromodulation and remote animal behavior control (*8, 10*). To activate tectal neurons in *Xenopus* tadpoles, the dissected optic tectum was incubated with DCSA-MOFs (10 μg/ml) in the extracellular saline and loaded with Fluo-8 (Fig. 5A). DCSA-MOFs were associated with the plasma membrane of tectal neurons, which had small soma (area: approximately 130 to 160 μm^2) (fig. S96). Low laser power at 488 nm (P_{laser} = 1.36 mW, 0.16 s) could repeatedly elicit Ca^{2+} responses in the same tectal neuron (Fig. 5B and fig. S97), whereas high laser power (P_{laser} = 2.27 mW, 0.16 s) induced ICWs in multiple neurons (Fig. 5C and fig. S98).

Excitatory synaptic transmission is a typical way of neuronal communication, in which the electrical impulse in a presynaptic neuron is conveyed to a postsynaptic neuron via the release of excitatory neurotransmitters. The dissected optic tectum containing DCSA-MOFs was irradiated by a 405-nm laser pointer (spot diameter: 1 cm), and miniature excitatory postsynaptic currents (mEPSCs) were recorded using an electrophysiology setup (fig. S99). To optimize laser power, tectal tissue was first exposed to six 30 s on/180 s off light cycles at different laser powers P_{laser} = 0.1 to 0.6 W. Figure S100 reveals that laser itself could not affect the mEPSC frequency in the absence of DCSA-MOFs, while coexistence of DCSA-MOFs and laser exposure (P_{laser} = 0.4 to 0.6 W) dramatically increased the mEPSC frequency. Then, the tectal was illuminated with three 30 s on/180 s off light cycles at a laser power P_{laser} = 0.4 W, and mEPSCs were recorded (Fig. 5D) and analyzed (fig. S101). Upon irradiation,

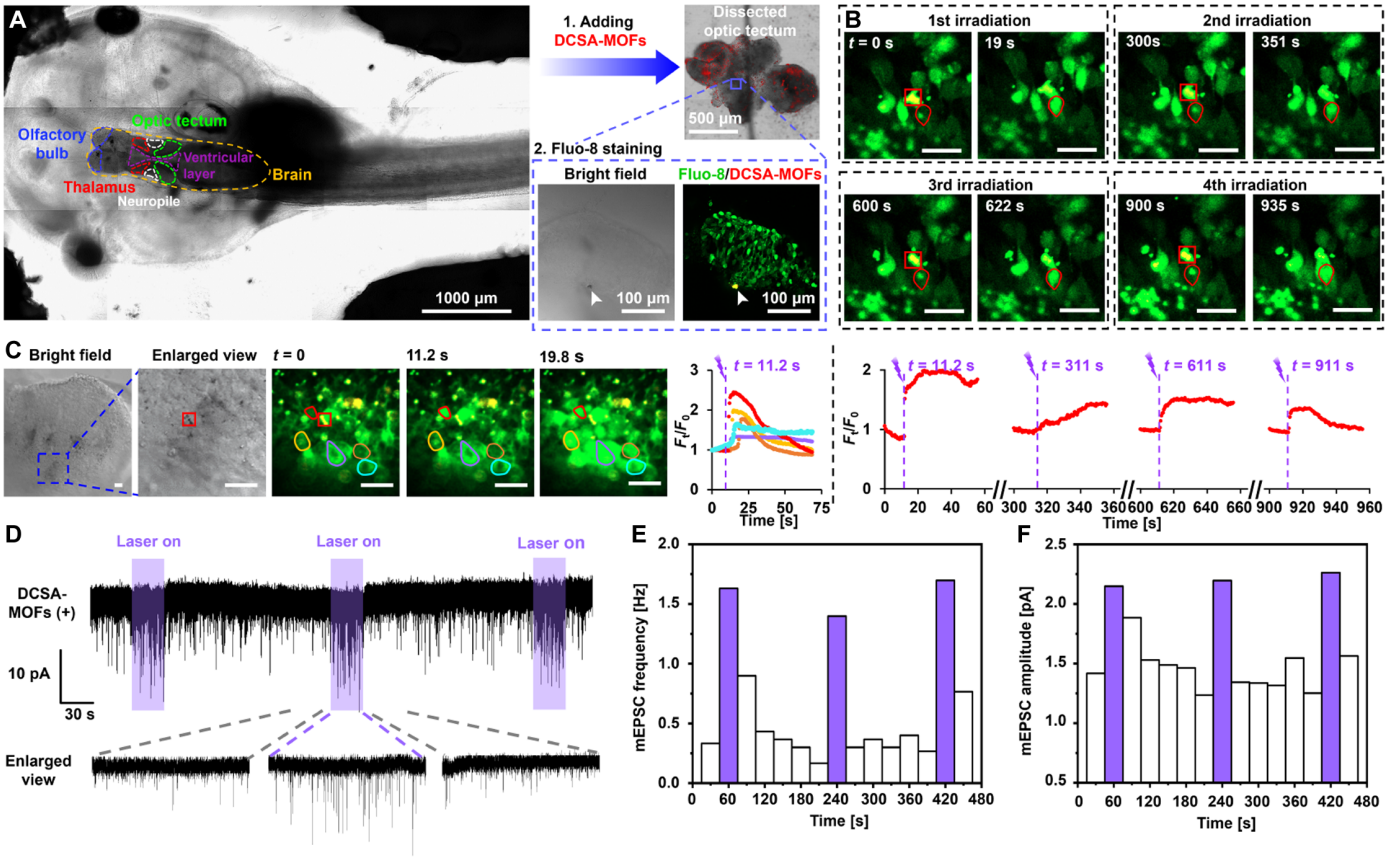

Fig. 5. Photoactivation of tectal neurons with membrane-associated DCSA-MOFs. (**A**) Schematic diagram of ex vivo optic tectum. DCSA-MOFs were indicated by white arrows. Fluo-8–stained neurons were shown in green. (**B** and **C**) Photoexcitation elicited Ca^{2+} responses. For photoexcitation, membrane-associated DCSA-MOFs in the red box were exposed to the 488-nm laser from CLSM at a laser power P_{laser} = (B) 1.36 mW or (C) 2.27 mW for 0.16 s. (B) Repetitive stimulation of a tectal neuron. The soma of the neuron outlined by the red line was stimulated four times every 5 min. (C) Photoexcitation triggered ICW propagation in tectal neurons. The curves with different colors indicate the Fluo-8 intensities of cells labeled by corresponding lines. Scale bar, 20 μm. (**D** to **F**) Electrophysiological activity of a neuron illuminated by a 405-nm laser pointer. (D) Traces of mEPSCs. Laser irradiation was performed with three 30 s on/180 s off cycles at a laser power P_{laser} = 0.4 W. Averaged mEPSC (E) frequency and (F) amplitude within 30 s as calculated from (D). Purple and white bars indicate the presence and absence of laser illumination, respectively.

the average mEPSC frequency in the tested neuron increased from 0.16 to 0.89 Hz to 1.40 to 1.70 Hz (Fig. 5E), and averaged mEPSC amplitudes increased from 1.24 to 1.88 pA to 2.15 to 2.26 pA (Fig. 5F). This is attributed to Ca^{2+}-mediated neurotransmitter release (*43*) and the resultant increase in synaptic strength (*44*). Of note, the mEPSCs returned to normal once the light was turned off. It was deduced that the extracellularly generated H_2O_2 could be rapidly diluted via diffusion into the surrounding extracellular medium, preventing its accumulation within the local area of photoexcited neurons (estimation can be referred to section S10.3).

Albino *Xenopus laevis* tadpoles can respond to the change in light. Tectal neurons receive direct excitatory retinal inputs within tectal circuits, and we hypothesized that stimulating tectal neurons would result in a visual avoidance behavior. Most DCSA-MOFs were located on the neurons in the optic tectum through ventricle injection, but not in the spinal cord (Fig. 6B). Then, the eyes and olfactory bulb, as the primary photoreceptors (*45*), were removed from tadpoles, rendering them less light-sensitive (Fig. 6A). Optic tectum receives and processes visual cues, which sends signals to hindbrain of reticulospinal neurons to initiate swimming behavior. The membrane-associated DCSA-MOFs generated H_2O_2 after photoexcitation, and the activation of tectal neurons by DCSA-MOFs mimics the integration of visual sensory inputs. Tectal cells projected to the hindbrain and synapse onto reticulospinal neurons. Few DCSA-MOFs were also associated with the hindbrain, which may contribute to motor coordination and balance. Reticulospinal neurons control tail movement by projecting to motor neurons and central pattern generators (CPGs) in the spinal cord. The heads of tadpoles were embedded in low melting agarose and illuminated with a 405-nm laser pointer at a laser power $P_{laser} = 0.4$ W until the tail began to sway, which was recorded with an optical microscope (Fig. 6, C and D, and movie S6). Two parameters, namely, the response latency and swaying frequency, were measured to evaluate the visual avoidance behavior. When both eyes and olfactory bulb were removed, the average latency was approximately 14.9 s, substantially longer than that of control tadpoles (latency: ~2.7 s) and those without eyes (latency: ~3.4 s) (Fig. 6E). Excitingly, the presence of DCSA-MOFs in tadpoles without eyes and olfactory bulbs significantly diminished the latency to the normal level (~3.3 s). There were no significant differences in the frequency (1.3 to 1.6 Hz; Fig. 6F) and duration (8.5 to 10.7 s) of tail movement among all tested groups. These results indicate that laser illumination of DCSA-MOFs could activate neurons and induce visual avoidance behavior.

Photoexcitation triggered thigh twitch in spinal frogs

To further investigate the potential of DCSA-MOFs to regulate animal motor behavior, the thigh of albino *X. laevis* frogs was remotely photoexcited. Figure 7A depicts a spinal frog model in which the brain was removed, but the spinal cord was well preserved for studying neural reflexes. The establishment of the spinal frog model was validated by rapid clawing after clamping the thigh with tweezers (fig. S103) or wiping the thigh with a 1 or 5 wt % H_2O_2 aqueous solution–soaked cotton (fig. S104). After subcutaneous injection of DCSA-MOF aqueous solution (200 μl, 5 mg/ml), the fluorescence of DCSA-MOFs was only observed in the injection site (Fig. 7B). The somatosensory neurons in the skin of *X. laevis* frogs could be activated by H_2O_2. The afferent nerve fibers in the sciatic nerve then transmit sensory information from somatosensory receptors to the spinal cord. Once the information has been processed, the efferent nerve fibers transport impulses from the spinal cord to the peripheral effector organs, namely, the skeletal muscles of the hindlimbs,

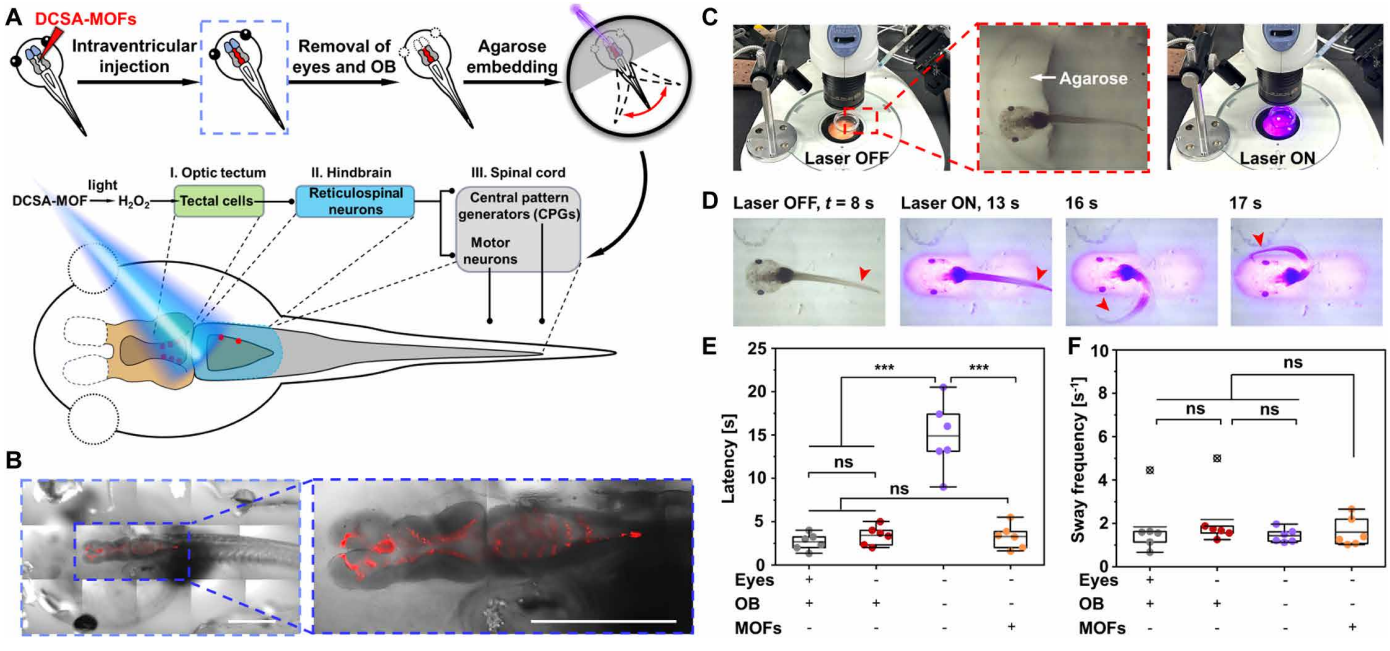

Fig. 6. Visual avoidance behavior of blind tadpoles induced by DCSA-MOFs under laser illumination. (**A** and **C**) Experimental procedures, activated neural circuits, and apparatus for regulating tadpole behaviors. (**B**) DCSA-MOF distributions in the ventricles after microinjection. DCSA-MOFs were shown in red. Scale bar, 1000 μm. (**D**) Snapshots extracted from a time-lapse video by an optical microscope showing the tail swaying in response to the laser. Arrows indicate the tail. (**E** and **F**) Sway (E) latency and (F) frequency of tested tadpoles during laser illumination ($n = 6$ tadpoles per group). Each tadpole was illuminated thrice. The points represent the average data from three times stimulation in one tadpole. ***$P < 0.001$; ns, no significant difference. OB, olfactory bulb.

and cause the wiping behavior. After cooling in the ice bath, the left thigh without DCSA-MOFs was exposed to a 405-nm laser pointer (spot diameter: 1 cm) at a laser power P_{laser} = 0.4 W for 127 s, and we did not observe the clawing behavior (Fig. 7, C and D). Upon irradiating the right thigh with injected DCSA-MOFs for 43 to 74 s, both legs twitched for 4 to 8 s. As measured by an infrared thermometer, surface temperature of the irradiated region did not exceed 30.1°C, below the TRPV1 activation threshold. Hence, the thermal effect was ruled out. Similar results were also observed in bullfrogs (Fig. 7, E to G, and movie S7). After irradiation for 54 s, the left thigh with injected DCSA-MOFs twitched seven times, whereas the right thigh without DCSA-MOFs only twitched once at the end of irradiation. These results reveal that photoexcitation of DCSA-MOFs could stimulate frog nerves and manipulate their locomotion behaviors.

DISCUSSION

The past decade has witnessed rapid advances in technologies that use light to manipulate cellular Ca^{2+} signaling, due to the urgent

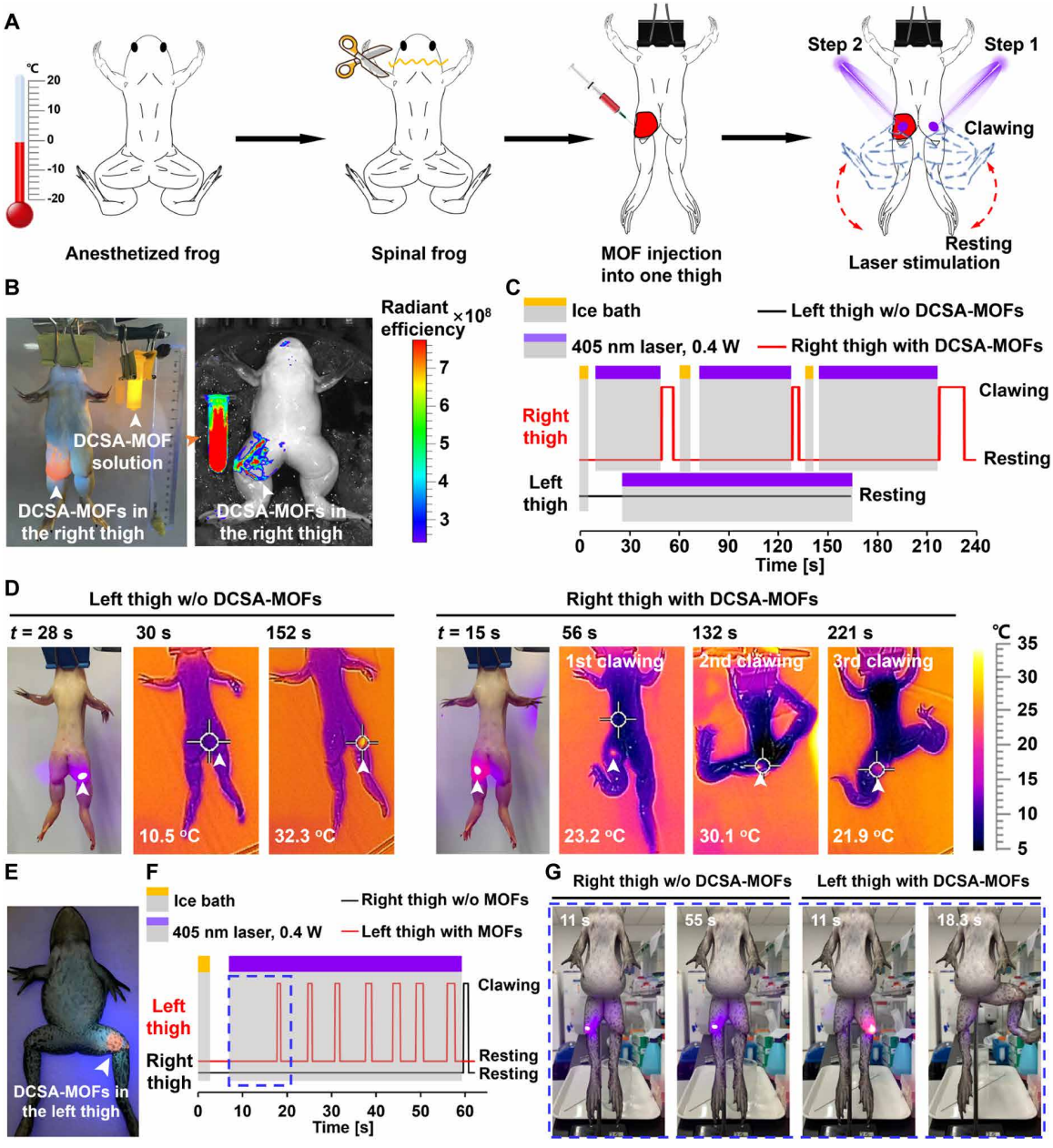

Fig. 7. Laser-driven remote regulation of spinal frogs. (**A**) Schematic illustration of experimental procedures. (**B**) In vivo distributions of DCSA-MOFs in an albino *X. laevis* frog. Left: a frog suspended vertically and illuminated by a 365-nm UV light. Right: the same frog lying on ice as captured by the IVIS Lumina II imaging system. (**C**) Plots of the clawing behavior of an albino *X. laevis* frog after laser irradiation on the left thigh without DCSA-MOFs and right thigh with DCSA-MOFs. (**D**) Snapshots and thermal imaging of the irradiated skin. White arrows represent the irradiated area. (**E** to **G**) Evaluation of behavioral control of a bullfrog using the same procedure.

need to deepen the understanding of Ca^{2+} signal–relevant physiological activities and treat Ca^{2+} disorder–induced diseases. Light can directly activate light-gated opsins (e.g., optogenetics) (*46*), thermal-gated TRPV1 channels via photothermal nanotransducers (*10*), or mechanosensitive TRPV4 channels by photoacoustic nanomaterials (*47*), thereby facilitating Ca^{2+} influx. These methods act on particular Ca^{2+} channels, necessitating their overexpression on specific cells or the use of genetic engineering techniques; this greatly restricts their applicability and raise concerns regarding biosafety and viral infection efficiency. An alternative approach involves encapsulating active biomolecules (e.g., IP_3 and SKF-81297) within thermal-sensitive (*48*) or light-sensitive (*49*) nanocarriers, and subsequently releasing them to stimulate specific targets upon light illumination. This approach also encountered the challenges of undesired premature leakage and restricted stimulation cycles.

ER, as the largest Ca^{2+} store in most eukaryotic cells, can release Ca^{2+} into the cytoplasm through the interaction of endogenous ROS and IP_3Rs. Here, we chose IP_3Rs as a potential stimulating target and leveraged a photocatalytic method to manipulate Ca^{2+} signaling. This design offered several advantages. (i) The application scope was dramatically expanded by the widespread overexpression of IP_3Rs in diverse cell types. (ii) Stimulating IP_3Rs with H_2O_2 was a safe and effective strategy, as H_2O_2 was considerably less toxic compared to other ROS. (iii) Photocatalytic production of H_2O_2 only consumed self-supplied H_2O and O_2, which prevented the consumption of loaded agents and drug leakage. (iv) DCSA-MOFs were stable inside cells, and H_2O_2 generation can be repeatedly switched on and off, enabling long-term controllable Ca^{2+} modulation.

Before further biological applications, it is necessary to consider the potential damage that H_2O_2 and Ca^{2+} overload could cause to the stimulated cells. The threshold concentration of H_2O_2 to evoke Ca^{2+} responses in HL-1 cells was determined to be 1 mM. Incubation of cells with 1 mM H_2O_2 for 24 or 48 hours resulted in a great reduction in cell viability by over 96% (fig. S67). Nonetheless, no discernible cytotoxicity was detected after cells with endocytosed DCSA-MOFs were photoexcited using either the confocal laser (fig. S61) or the external laser pointer (fig. S63). Besides, HL-1 cells (Fig. 3D and fig. S59), tectal neurons (Fig. 5B), and thigh of spinal frogs (Fig. 7, D and G) have been demonstrated to be repeatedly activated at least three times, which proved that our modulation strategy was safe. This is because we have optimized the laser power and irradiation time to avoid generating excess H_2O_2. According to the calculation in section S8.5, the amount of photosynthesized H_2O_2 in a single cell after a single photoexcitation was about 2.03×10^{-16} mol. The local concentration of H_2O_2 at the nearest ER was estimated to be 1.13 M, which was three orders of magnitudes above the activation threshold. After diffusion into the extracellular medium, the H_2O_2 concentration was only 1.35×10^{-2} μM, a value unable to cause cell damage (fig. S67). Hence, the method by which cells were stimulated with extracellular H_2O_2 differed from the in situ localized H_2O_2 photogeneration process. In the previous scenario, extracellular medium contained abundant H_2O_2, ensuring that cells were consistently stimulated with such H_2O_2 concentrations. In the latter scenario, locally produced H_2O_2 concentration was adequate to activate the IP_3Rs of nearby ERs; H_2O_2 could subsequently diffuse out of cells and become highly diluted in the extracellular medium, thereby rendering it nontoxic. Additionally, we excluded the potentiality of Ca^{2+} overload–induced mitochondrial dysfunction by using the JC-1 probe to detect the mitochondrial membrane potentials. No detectable change in fluorescence was found between photoexcited cells and nonexcited cells (figs. S62 and S64). This is likely that the transient elevation in $[Ca^{2+}]_{cyto}$ (lasting for less than 140 s; fig. S59) was insufficient to induce damage to the mitochondria.

One limitation of our approach is that the 405-nm light was used. Despite numerous studies asserting that existing photocatalysts, such as graphitic carbon nitride (g-C_3N_4), TiO_2 photocatalysts, and covalent organic frameworks (COFs), could efficiently photosynthesize H_2O_2 under simulated sunlight, their optimal operating wavelength was below 500 nm and, in some cases, ultraviolet (UV) light (*19, 50*). Visible light with such a short wavelength raises concerns regarding limited tissue penetration, undesired photothermal heating effect due to inherent absorption by endogenous chromophores, and the induction of ROS and inflammation at high laser energy (*51*), which can be detrimental to organisms. On the basis of our calculation, the optimized irradiation parameters for in vivo applications are within the acceptable extent, thereby preventing organism damage (section S10.7). It has been reported that photocatalysts doped with carbon dots (*52*) or conjugated with palladium(II) mesotetraphenylte-trabenzoporphyrin (*53*) effectively extended the working wavelength to 630 to 660 nm. Utilization of such materials may present a viable avenue for enhancing our system.

Owing to the importance of cellular Ca^{2+} signaling regulation, we anticipate that this system will have broad applications, especially for neurodevelopment research, regulation of immune system, treatment of central nervous system (CNS) diseases, Ca^{2+}-mediated gene expression, secretion of bioactive materials, and Ca^{2+} overload–induced cancer therapy. For instance, incorporating Ca^{2+}/NFAT (nuclear factor of activated T cells) pathway into cells represents a promising method to control gene expression. Gene constructs can be designed by placing transcription factor NFAT on the upstream of target gene. After cells are transfected by those genes, an increment in $[Ca^{2+}]_{cyto}$ will initiate the expression of target gene for biological functions, such as blood glucose regulation (*54*) and thrombolysis treatment (*55*).

Consequently, we here developed 9,10-distyrylanthracene as an organic photocatalyst that efficiently generated H_2O_2 under xenon light illumination. To increase payload efficiency and biocompatibility, and amplify photocatalytic activity, its derivative DCSA was then coupled with Zr_6 cluster to prepare submicrometer MOFs (DCSA-MOFs). In 2D and 3D cell culture models, DCSA-MOFs exhibited excellent cellular Ca^{2+} manipulation activity. The prepared DCSA-MOF has been proven to regulate visual avoidance behavior in blind tadpoles and thigh twitch in spinal frogs.

MATERIALS AND METHODS

All experimental details are described in the Supplementary Materials. Only some of them are described here.

Constructions of DCSA-MOFs

A solution of $ZrOCl_2 \cdot 8H_2O$ (10 mg, 0.03 mmol, 1 eq, #E010555, Energy Chemical), DCSA (23.5 mg, 0.05 mmol, 1.67 eq), and benzoic acid (100 mg, 0.82 mmol, 27.3 eq, #W810151, Energy Chemical) in *N*,*N*-dimethylformamide (DMF; 8 ml) was stirred at 300 rpm at 90°C for 48 hours under N_2 atmosphere. The mixture was centrifuged at 9500*g* for 5 min, and the sediment was washed with DMF (3 × 5 ml) and then with ethanol (3 × 5 ml), respectively. That is, the sediment was resuspended in DMF or EtOH by sonication, the mixture was

centrifuged at 9500*g* for 5 min, and the supernatant was removed. The purified DCSA-MOFs were dried under vacuum at 50°C to obtain a yellow powder (11.5 mg, 33.7% yield).

The protocol for evoking cytosolic Ca^{2+} response and detecting $[Ca^{2+}]_{cyto}$

Fluo-8 AM can diffuse into cell cytosol and be hydrolyzed to Fluo-8 by endogenous esterase. Fluo-8 is then entrapped within cells for $[Ca^{2+}]_{cyto}$ detection. One vial of Fluo-8 AM (#MX4505, Shanghai Maokang Biotechnology, 50 μg) was dissolved in 30 μl of anhydrous dimethyl sulfoxide (DMSO) to prepare 1.5 mM stock solution. Anhydrous DMSO was obtained by soaking with calcium hydride (#C108375, Shanghai Aladdin Bio-Chem Technology Co. Ltd.) for at least 4 days. After a brief centrifugation, anhydrous DMSO was taken out. According to our experience, the stock solution of Fluo-8 AM in DMSO should be stored at −20°C and used within 2 weeks before its hydrolysis and subsequent loss of cell loading capacity. The staining solution consisted of 1 μl of Fluo-8 AM stock solution (1.5 mM in anhydrous DMSO), 1 μl of Pluronic F-127 (#MS4301, Shanghai Maokang Biotechnology) (6 wt % in DMSO), and 300 μl of HBSS. Of note, some cells with a limited tolerance for Fluo-8 AM should be stained at lower concentrations. After taking up DCSA-MOFs, cells were then washed three times with HBSS and incubated for 30 min with freshly prepared staining solution. After two washes with HBSS, cells were imaged by CLSM900 (excitation, 488 nm/emission, 520 nm). To photoexcite DCSA-MOFs within a custom-made region, the "Experiment Regions" and "Bleaching" modules in the ZEN 3.3 blue edition software were used. The mean irradiation time was $\Delta t_{laser} = 0.16$ s, and a typical irradiation area was $A_{laser} = 15.2\ \mu m^2$. Note that A_{laser} values were slightly changed based on the actual situation. Both parameters can be directly read from ZEN 3.3 black edition software in the "Gallery" and "Graphics" modules, respectively. The maximum laser power was used for photoexcitation; the corresponding parameters are shown below: laser power $P_{laser} = 2.27$ mW, power density $I_{laser} = 1.49 \times 104\ W/cm^2$; energy $E_{laser} = 0.363$ mJ; energy density $U_{laser} = 2.39 \times 103\ J/cm^2$. DCSA-MOFs were irradiated only in the custom-made regions at the sixth frames. The data were analyzed by MATLAB2019a. Fluorescence was normalized to the average value calculated from the first five images.

Triggering propagation of ICWs in cocultured MCF-7 and HL-1 cells by photoexcitation

MCF-7 and HL-1 cells were cocultured to determine whether a single cell can transmit Ca^{2+} signals to a distinct cell type. Briefly, 150,000 HL-1 cells or 320,000 MCF-7 cells in 2 ml of 10% FBS–supplemented Dulbecco's modified Eagle's medium (DMEM) were separately seeded in a six-well plate (seeding area: 9.5 cm^2) and incubated overnight. On the next day, the medium was removed, and cells were incubated with 2 ml of DCSA-MOFs (10 μg/ml) in 10% FBS–supplemented DMEM for 24 hours. To distinguish different cell types, MCF-7 cells were labeled by CellTracker Red CMTPX (#MX4109, Shanghai Maokang Biotechnology). To prepare the staining solution, 2 μl of CellTracker Red CMTPX (2 mM) in dry DMSO was diluted with 1 ml of HBSS. MCF-7 cells were washed three times with HBSS and incubated with the staining solution at 37°C for 35 min. Cells were then washed three times with phosphate-buffered saline (PBS), trypsinized by 0.25 wt % trypsin, and resuspended in cell culture medium containing 10% FBS. MCF-7 and HL-1 cells were mixed at a ratio of 4:1 for coculture. In each well of the eight-well chambered cover glass (seeding area: 0.81 cm^2), 40,000 cells were seeded. After 24 hours of incubation, cells were stained with Fluo-8 AM. A single MCF-7 or HL-1 cell was irradiated at 488 nm (20× objective, CLSM900) at a laser power $P_{laser} = 2.27$ mW for irradiation time $\Delta t_{laser} = 0.16$ s to evoke Ca^{2+} response and then imaged.

Spheroid culture

Spheroids between 120 and 150 μm in diameter were prepared via a hanging drop method according to our previous reported protocol (*35*). Briefly, 150,000 HL-1 cells or 320,000 MCF-7 cells in 2 ml of 10% FBS–supplemented DMEM were seeded in a six-well plate (seeding area: 9.5 cm^2) and incubated overnight. On the next day, the medium was removed, and cells were incubated with 2 ml of DCSA-MOFs (10 μg/ml) in 10% FBS–supplemented DMEM for 24 hours. To visualize spheroids under CLSM, HL-1 and MCF-7 cells were labeled with CellTracker Red CMTPX and CellTracker Deep Red, respectively. Cells were then washed three times with PBS, trypsinized by 0.25 wt % trypsin, and resuspended in cell culture medium containing 10% FBS. To prepare spheroids, 100,000 cells in 3 ml of cell culture medium were mixed with 1 ml of 1.2 wt % methylcellulose (viscosity: 4000 cP, #M0512, Sigma-Aldrich) aqueous solution. Cell suspension (20 μl) was added onto the inner face of the lid of a petri dish (area: 176.7 cm^2) by multichannel pipettes. To prevent cell suspension from evaporation, MilliQ water was added to the bottom of the petri dish, and the lid was inverted. HL-1 cells were incubated for 18 to 24 hours to form spheroids, while MCF-7 cells were incubated for 84 to 96 hours.

Triggering $[Ca^{2+}]_{cyto}$ increase in HL-1 multicellular spheroids by photoexcitation

For staining, 80 to 100 HL-1 spheroids were collected into a 15-ml Eppendorf tube and centrifuged at 1200 rpm (200*g*) for 90 s. The supernatant was carefully removed, and 4 to 5 ml of HBSS solution were gently added. The mixture was gently inverted and centrifuged again at 1200 rpm (200*g*) for 90 s. This process was repeated twice until the supernatant was almost colorless. Spheroids were then transferred to one well of a 24-well plate, whose bottom was precoated with 400 μl of 1.0 wt % agarose gel to prevent the spheroids from adhering to the bottom of the plate. For staining, spheroids were incubated in a staining solution at 37°C for 80 to 90 min. The staining solution consisted of 4 μl of 1.5 mM Cal-520 AM solution in DMSO (#MX4537, Shanghai Maokang Biotechnology), 2 μl of Pluronic F-127 (#MS4301, Shanghai Maokang Biotechnology), and 800 μl of 0.94 mM probenecid (#P129440, Shanghai Aladdin Bio-Chem Technology Co. Ltd.) in HBSS. On the basis of our experience, Cal-520 AM is superior to Fluo-8 AM for Ca^{2+} staining in 3D cell culture. Then, spheroids suspended in 150 μl of staining solution were transferred to one well of an eight-well chambered cover glass. Cells that were 30 to 45 μm away from the top of spheroids in the *z* direction were imaged.

Triggering Ca^{2+} signaling in optic tectum

Albino *X. laevis* tadpoles were anesthetized with 0.02 wt % MS-222 in Steinberg's solution for approximately 2 min or until loss of reflex responses. First, we attempted in situ staining of tectal neurons by injecting Ca^{2+} indicators [e.g., Fluo-8 AM or Oregon Green 488 BAPTA-1 AM (#20507, Shanghai Maokang Biotechnology)] directly

into the optical tectum of tadpole brain via a puncture micropipette. However, fluorescence was restricted to a small region surrounding the injection site, indicating that the staining was heterogeneous. We then tried ex vivo staining method. Figure 5A depicts the flowchart. The entire brain tissue was carefully dissected under a microscope, immersed in 1 ml of the extracellular saline (115 mM NaCl, 2 mM KCl, 3 mM $CaCl_2$, 1.5 mM $MgCl_2$, 5 mM Hepes, 10 mM glucose, and 0.01 mM glycine, pH 7.2, osmolality 255 mOsm), and fixed in a custom-made petri dish to prevent it from floating. Because of the inability of tectal neurons to endocytose DCSA-MOFs, brain tissue was incubated with 10 μl of DCSA-MOF aqueous solution (1 mg/ml), allowing DCSA-MOFs to associate with the outer membrane of superficial cells. Tectal neurons were stained with Fluo-8 AM (5 μM) in extracellular saline at room temperature for 40 min. Like 3D multicellular spheroids, only cells near the tissue surface can be fully stained.

To exclude the possibility of spontaneous spiking of neurons, cells were imaged for 25 frames every 0.635 s before photoexcitation. As shown in fig. S96, DCSA-MOFs associated with plasma membrane can be observed in the bright field and was photoexcited at 488 nm (20× objective, LSM900) at a laser power P_{laser} = 2.27 mW for irradiation time Δt_{laser} = 0.16 s. The Ca^{2+} signals were recorded for 150 fames by CLSM900. The data were analyzed by MATLAB2019a using a custom script.

Visual avoidance assay of *X. laevis* tadpole

Albino *X. laevis* tadpoles avoid intense light and prefer dark environment. Currie *et al.* (*45*) report that a photosensitive tissue in the caudal diencephalon of a tadpole is sensitive to short-wavelength UV light (390 to 410 nm) so that a tadpole lacking lateral eyes could still elicit a robust locomoting response under illumination. For laser stimulation, we removed the eyes and olfactory bulb, which contained diencephalon. Albino *X. laevis* tadpoles were anesthetized with 0.02 wt % MS-222 in Steinberg's solution for approximately 2 min or until loss of reflex responses. Here, tadpoles were divided into four groups (n = 6 for each group): (i) group 1: tadpoles with eyes and olfactory bulb but without DCSA-MOFs; (ii) group 2: tadpole with olfactory bulb, but without eyes and DCSA-MOFs; (iii) group 3: tadpoles without eyes, olfactory bulb, and DCSA-MOFs; (iv) group 4: tadpoles without eyes and olfactory bulb, but with intraventricularly injected DCSA-MOFs (1 mg/ml, 50 nl). The eyes and olfactory bulb were carefully removed using a stereomicroscope. Tadpoles were given approximately 60 min to recover from surgery and injection. The heads of tadpoles were then embedded in 1.5 wt % agarose with a low melting point (#5265, Agarose LM SIEVE, Takara) in a custom-made imaging chamber, whereas their tails were free to move in the Steinberg's solution under illumination. The agarose melts at 65.5°C, remains fluid at 37°C, and forms gels rapidly below 25°C. Tadpoles were photographed by a high-speed camera to observe the tail wagging. A tadpole was first imaged for at least 12 s to ensure that its tail did not move. Then, their head was illuminated by a 405-nm laser at a laser power P_{laser} = 0.4 W for several seconds, and the laser was turned off for more than 20 s until the tail ceased wagging for at least 10 s. The procedure was repeated three times in each tadpole, and the average response time and wagging frequency from three repetitions were determined.

Establishment of a spinal frog model

The albino *Xenopus* frogs were anesthetized by injecting tricaine (0.3 ml of 5% solution) and placed on ice to accelerate the anesthetic effect. To prepare spinal frogs, frogs were wrapped in cloth, and the upper jaw was cut off with surgical scissors. Frogs were suspended to the tripod by clamping their lower jaws. The response of spinal frogs to touch was then evaluated. When the right toes, crus, or thigh was clamped with tweezers, the right leg bended first, followed by the left leg (fig. S103). After several seconds, the frogs resumed their resting state. This result demonstrates that spinal frogs can respond to external stimuli and engage in clawing behavior.

Optical modulation of spinal frogs after subcutaneous injection of DCSA-MOFs

To evaluate whether laser irradiation can elicit a behavioral response, DCSA-MOF aqueous solution (200 μl, 5 mg/ml) was injected subcutaneously into the right thigh of the frog, whereas the left thigh was injected with Ringer solution as a control. To measure the biodistributions of injected DCSA-MOFs, we first used a UV light (365 nm, 5 W) to illuminate a suspended frog in a tripod, and images were captured by a mobile phone. Because of limited tissue penetration of UV light, only the superficial distribution of DCSA-MOFs was visible. Afterward, the IVIS Lumina II system (PerkinElmer, USA) was used to observe the in vivo distribution of the same frog that lied on ice.

Optical modulation of spinal frogs was conducted according to others' protocol (*56*) with modifications. Both thighs were cooled by immersing in the ice-cold water for 7 s. The purpose is to eliminate the laser-induced thermal effect, which can cause a reflexive bending of the leg. The left thigh was initially treated with a 405-nm laser beam (spot diameter: 1 cm) at a laser power P_{laser} = 0.4 W for irradiation time Δt_{laser} = 127 s. Both thighs were cooled again by immersing in the ice-cold water for 7 s. The injection location on the right thigh was then exposed to a 405-nm laser with a laser power P_{laser} = 0.4 W for irradiation time Δt_{laser} = 44 to 70 s until the frog began to move. This procedure was repeated three times. Simultaneously, the surface temperature of the irradiated area was monitored by an infrared thermometer (A-BF RX-680 Infrared Thermal Imager). The experiment was also performed on bullfrogs using the same protocol.

Statistical analysis

All data were analyzed by one-way analysis of variance (ANOVA) with Tukey's correction. ***$P < 0.001$, **$P < 0.01$, and *$P < 0.05$ were considered to indicate a significant difference; ns was considered to indicate a no significant difference. Statistical tests were performed with Origin 2023 software.

Supplementary Materials

This PDF file includes:

Sections S1 to S11
Figs. S1 to S108
Tables S1 to S6
Legends for movies S1 to S7
References

Other Supplementary Material for this manuscript includes the following:

Movies S1 to S7

REFERENCES AND NOTES

1. D. E. Clapham, Calcium signaling. *Cell* **131**, 1047–1058 (2007).
2. M. Tsutsumi, K. Inoue, S. Denda, K. Ikeyama, M. Goto, M. Denda, Mechanical-stimulation-evoked calcium waves in proliferating and differentiated human keratinocytes. *Cell Tissue Res.* **338**, 99–106 (2009).

3. J. Mo, Y. Xu, X. Wang, W. Wei, J. Zhao, Exploiting the protein corona: Coating of black phosphorus nanosheets enables macrophage polarization via calcium influx. *Nanoscale* **12**, 1742–1748 (2020).
4. Y. Pan, S. Yoon, J. Sun, Z. Huang, C. Lee, M. Allen, Y. Wu, Y.-J. Chang, M. Sadelain, K. K. Shung, Mechanogenetics for the remote and noninvasive control of cancer immunotherapy. *Proc. Natl. Acad. Sci. U.S.A.* **115**, 992–997 (2018).
5. D. Rosenfeld, A. W. Senko, J. Moon, I. Yick, G. Varnavides, D. Gregureć, F. Koehler, P.-H. Chiang, M. G. Christiansen, L. Y. Maeng, Transgene-free remote magnetothermal regulation of adrenal hormones. *Sci. Adv.* **6**, eaaz3734 (2020).
6. J. Yuan, H. Liu, H. Zhang, T. Wang, Q. Zheng, Z. Li, Controlled activation of TRPV1 channels on microglia to boost their autophagy for clearance of alpha-synuclein and enhance therapy of Parkinson's disease. *Adv. Mater.* **34**, e2108435 (2022).
7. J. L. Beckham, A. R. van Venrooy, S. Kim, G. Li, B. Li, G. Duret, D. Arnold, X. Zhao, J. T. Li, A. L. Santos, Molecular machines stimulate intercellular calcium waves and cause muscle contraction. *Nat. Nanotech.* **18**, 1051–1059 (2023).
8. C. Sebesta, D. Torres Hinojosa, B. Wang, J. Asfouri, Z. Li, G. Duret, K. Jiang, Z. Xiao, L. Zhang, Q. Zhang, Subsecond multichannel magnetic control of select neural circuits in freely moving flies. *Nat. Mater.* **21**, 951–958 (2022).
9. P. Li, J. Zhang, H. Hayashi, J. Yue, W. Li, C. Yang, C. Sun, J. Shi, J. Huberman-Shlaes, N. Hibino, Monolithic silicon for high spatiotemporal translational photostimulation. *Nature* **626**, 990–998 (2024).
10. X. Wu, Y. Jiang, N. J. Rommelfanger, F. Yang, Q. Zhou, R. Yin, J. Liu, S. Cai, W. Ren, A. Shin, Tether-free photothermal deep-brain stimulation in freely behaving mice via wide-field illumination in the near-infrared-II window. *Nat. Biomed. Eng.* **6**, 754–770 (2022).
11. X. Chu, X. Jiang, Y. Liu, S. Zhai, Y. Jiang, Y. Chen, J. Wu, Y. Wang, Y. Wu, X. Tao, Nitric oxide modulating calcium store for Ca^{2+}-initiated cancer therapy. *Adv. Funct. Mater.* **31**, 2008507 (2021).
12. J. K. Foskett, C. White, K.-H. Cheung, D.-O. D. Mak, Inositol trisphosphate receptor Ca^{2+} release channels. *Physiol. Rev.* **87**, 593–658 (2007).
13. S. K. Joseph, M. P. Young, K. Alzayady, D. I. Yule, M. Ali, D. M. Booth, G. Hajnóczky, Redox regulation of type-I inositol trisphosphate receptors in intact mammalian cells. *J. Biol. Chem.* **293**, 17464–17476 (2018).
14. Y. Zheng, X. Shen, H2O2directly activates inositol 1,4,5-trisphosphate receptors in endothelial cells. *Redox Rep.* **10**, 29–36 (2005).
15. C. C. Winterbourn, Reconciling the chemistry and biology of reactive oxygen species. *Nat. Chem. Biol.* **4**, 278–286 (2008).
16. L.-S. Lin, T. Huang, J. Song, X.-Y. Ou, Z. Wang, H. Deng, R. Tian, Y. Liu, J.-F. Wang, Y. Liu, Synthesis of copper peroxide nanodots for H2O2Self-Supplying chemodynamic therapy. *J. Am. Chem. Soc.* **141**, 9937–9945 (2019).
17. C. Wang, J. Yang, C. Dong, S. Shi, Glucose oxidase-related cancer therapies. *Adv. Ther.* **3**, 2000110 (2020).
18. J. He, L.-H. Fu, C. Qi, J. Lin, P. Huang, Metal peroxides for cancer treatment. *Bioact. Mater.* **6**, 2698–2710 (2021).
19. Z. Yong, T. Ma, Solar-to-H_2O_2 catalyzed by covalent organic frameworks. *Angew. Chem. Int. Ed.* **135**, e202308980 (2023).
20. Y. Zhao, X. Li, X. Fan, H. Wang, Y. Liu, Y. Chen, T. Yang, J. Ye, H. Huang, H. Li, Small-molecule catalyzed H_2O_2 production via a phase-transfer photocatalytic process. *Appl. Catal. B Environ.* **314**, 121499 (2022).
21. Z. Wu, X. Li, Y. Zhao, Y. Li, K. Wei, H. Shi, T. Zhang, H. Huang, Y. Liu, Z. Kang, Organic semiconductor/carbon dot composites for highly efficient hydrogen and hydrogen peroxide coproduction from water photosplitting. *ACS Appl. Mater. Interfaces* **13**, 60561–60570 (2021).
22. D. Zhu, H. Yan, Y. Zhou, L. M. Nack, J. Liu, W. J. Parak, Design of disintegrable nanoassemblies to release multiple small-sized nanoparticles. *Adv. Drug Deliv. Rev.* **197**, 114854 (2023).
23. Z. Hu, Y. Li, M. Kang, M. M. Islam, M. Chen, J. Zhang, Y. Xiao, X. Feng, C. Redshaw, M. Zhang, Aggregation-induced emission luminogen: A new perspective in the photo-degradation of organic pollutants. *EcoMat* **2**, e12024 (2020).
24. V. Hanková, E. Slováková, J. Zedník, J. Vohlídal, R. Sivkova, H. Balcar, A. Zukal, J. Brus, J. Sedláček, Polyacetylene-type networks prepared by coordination polymerization of diethynylarenes: New type of microporous organic polymers. *Macromol. Rapid Commun.* **33**, 158–163 (2012).
25. B. Yang, Y. Chen, J. Shi, Reactive oxygen species (ROS)-based nanomedicine. *Chem. Rev.* **119**, 4881–4985 (2019).
26. L. Yang, G. Dong, D. L. Jacobs, Y. Wang, L. Zang, C. Wang, Two-channel photocatalytic production of H_2O_2 over g-C_3N_4 nanosheets modified with perylene imides. *J. Catal.* **352**, 274–281 (2017).
27. C. Wu, Z. Teng, C. Yang, F. Chen, H. B. Yang, L. Wang, H. Xu, B. Liu, G. Zheng, Q. Han, Polarization engineering of covalent triazine frameworks for highly efficient photosynthesis of hydrogen peroxide from molecular oxygen and water. *Adv. Mater.* **34**, e2110266 (2022).
28. H. Li, Y. Li, L. Sun, S. Xun, W. Jiang, M. Zhang, W. Zhu, H. Li, H_2O_2 decomposition mechanism and its oxidative desulfurization activity on hexagonal boron nitride monolayer: A density functional theory study. *J. Mol. Graph. Model.* **84**, 166–173 (2018).
29. A. Kulkarni, S. Siahrostami, A. Patel, J. K. Nørskov, Understanding catalytic activity trends in the oxygen reduction reaction. *Chem. Rev.* **118**, 2302–2312 (2018).
30. S. Wang, Z. Xie, D. Zhu, S. Fu, Y. Wu, H. Yu, C. Lu, P. Zhou, M. Bonn, H. I. Wang, Efficient photocatalytic production of hydrogen peroxide using dispersible and photoactive porous polymers. *Nat. Commun.* **14**, 6891 (2023).
31. C. Zhao, X. Wang, Y. Yin, W. Tian, G. Zeng, H. Li, S. Ye, L. Wu, J. Liu, Molecular level modulation of anthraquinone-containing resorcinol-formaldehyde resin photocatalysts for H_2O_2 production with exceeding 1.2% efficiency. *Angew. Chem. Int. Ed.* **62**, e202218318 (2023).
32. M. S. Giambelluca, O. A. Gende, Hydrogen peroxide activates calcium influx in human neutrophils. *Mol. Cell. Biochem.* **309**, 151–156 (2008).
33. M. P. Granados, G. M. Salido, A. González, J. A. Pariente, Dose-dependent effect of hydrogen peroxide on calcium mobilization in mouse pancreatic acinar cells. *Biochem. Cell Biol.* **84**, 39–48 (2006).
34. A. Laporte, S. Lortz, C. Schaal, S. Lenzen, M. Elsner, Hydrogen peroxide permeability of cellular membranes in insulin-producing cells. *Biochim. Biophys. Acta-Biomembr.* **1862**, 183096 (2020).
35. D. Zhu, L. Feng, N. Feliu, A. H. Guse, W. J. Parak, Stimulation of local cytosolic calcium release by photothermal heating for studying intra- and intercellular calcium waves. *Adv. Mater.* **33**, e2008261 (2021).
36. N. Brkovic, L. Zhang, J. N. Peters, S. Kleine-Doepke, W. J. Parak, D. Zhu, Quantitative assessment of endosomal escape of various endocytosed polymer-encapsulated molecular cargos upon photothermal heating. *Small* **16**, e2003639 (2020).
37. S. Györke, M. Fill, Ryanodine receptor adaptation: Control mechanism of Ca^{2+}-induced Ca^{2+} release in heart. *Science* **260**, 807–809 (1993).
38. W. Wang, X. Wu, K. W. Kevin Tang, I. Pyatnitskiy, R. Taniguchi, P. Lin, R. Zhou, S. L. C. Capocyan, G. Hong, H. Wang, Ultrasound-triggered in situ photon emission for noninvasive optogenetics. *J. Am. Chem. Soc.* **145**, 1097–1107 (2023).
39. F. Ceriani, T. Pozzan, F. Mammano, Critical role of ATP-induced ATP release for Ca^{2+} signaling in nonsensory cell networks of the developing cochlea. *Proc. Natl. Acad. Sci. U.S.A.* **113**, E7194–E7201 (2016).
40. J. A. Orellana, H. A. Sánchez, K. A. Schalper, V. Figueroa, J. C. Sáez, Regulation of intercellular calcium signaling through calcium interactions with connexin-based channels. *Calcium Signal.*, 777–794 (2012).
41. C. Giaume, L. Venance, Intercellular calcium signaling and gap junctional communication in astrocytes. *Glia* **24**, 50–64 (1998).
42. S. K. Rastogi, R. Garg, M. G. Scopelliti, B. I. Pinto, J. E. Hartung, S. Kim, C. G. Murphey, N. Johnson, D. San Roman, F. Bezanilla, Remote nongenetic optical modulation of neuronal activity using fuzzy graphene. *Proc. Natl. Acad. Sci. U.S.A.* **117**, 13339–13349 (2020).
43. W. A. Catterall, A. P. Few, Calcium channel regulation and presynaptic plasticity. *Neuron* **59**, 882–901 (2008).
44. N. Schwartz, A. Schohl, E. S. Ruthazer, Neural activity regulates synaptic properties and dendritic structure in vivo through calcineurin/NFAT signaling. *Neuron* **62**, 655–669 (2009).
45. S. P. Currie, G. H. Doherty, K. T. Sillar, Deep-brain photoreception links luminance detection to motor output in Xenopus frog tadpoles. *Proc. Natl. Acad. Sci. U.S.A.* **113**, 6053–6058 (2016).
46. A. Pliss, T. Y. Ohulchanskyy, G. Chen, J. Damasco, C. E. Bass, P. N. Prasad, Subcellular optogenetics enacted by targeted nanotransformers of near-infrared light. *ACS Photonics* **4**, 806–814 (2017).
47. Y. Jiang, Y. Huang, X. Luo, J. Wu, H. Zong, L. Shi, R. Cheng, Y. Zhu, S. Jiang, L. Lan, Neural stimulation in vitro and in vivo by photoacoustic nanotransducers. *Matter* **4**, 654–674 (2021).
48. H. Xiong, X. Li, P. Kang, J. Perish, F. Neuhaus, J. E. Ploski, S. Kroener, M. O. Ogunyankin, J. E. Shin, J. A. Zasadzinski, Near-infrared light triggered-release in deep brain regions using ultra-photosensitive nanovesicles. *Angew. Chem. Int. Ed.* **59**, 8608–8615 (2020).
49. H. Xiong, K. A. Alberto, J. Youn, J. Taura, J. Morstein, X. Li, Y. Wang, D. Trauner, P. A. Slesinger, S. O. Nielsen, Optical control of neuronal activities with photoswitchable nanovesicles. *Nano Res.* **1-9**, 1 (2022).
50. Y. Guo, X. Tong, N. Yang, Photocatalytic and electrocatalytic generation of hydrogen peroxide: Principles, catalyst design and performance. *Nano-Micro Lett.* **15**, 77 (2023).
51. K. P. Lawrence, T. Douki, R. P. Sarkany, S. Acker, B. Herzog, A. R. Young, The UV/visible radiation boundary region (385–405 nm) damages skin cells and induces "dark" cyclobutane pyrimidine dimers in human skin in vivo. *Sci. Rep.* **8**, 12722 (2018).
52. X. Fang, S. Cai, M. Wang, Z. Chen, C. Lu, H. Yang, Photogenerated holes mediated nitric oxide production for hypoxic tumor treatment. *Angew. Chem. Int. Ed.* **60**, 7046–7050 (2021).

53. S. Tao, Z. Shen, J. Chen, Z. Shan, B. Huang, X. Zhang, L. Zheng, J. Liu, T. You, F. Zhao, Red light-mediated photoredox catalysis triggers nitric oxide release for treatment of cutibacterium acne induced intervertebral disc degeneration. *ACS Nano* **16**, 20376–20388 (2022).
54. S. A. Stanley, J. E. Gagner, S. Damanpour, M. Yoshida, J. S. Dordick, J. M. Friedman, Radio-wave heating of iron oxide nanoparticles can regulate plasma glucose in mice. *Science* **336**, 604–608 (2012).
55. D. Zhang, C. Zhang, S. Lan, Y. Huang, J. Liu, J. Li, X. Liu, H. Yang, Near-infrared light activated thermosensitive ion channel to remotely control transgene system for thrombolysis therapy. *Small* **15**, e1901176 (2019).
56. E. Miyako, J. Russier, M. Mauro, C. Cebrian, H. Yawo, C. Ménard-Moyon, J. A. Hutchison, M. Yudasaka, S. Iijima, L. De Cola, Photofunctional nanomodulators for bioexcitation. *Angew. Chem. Int. Ed.* **53**, 13121–13125 (2014).
57. Y.-P. Ou, J. Zhang, Y. Hu, J. Yin, C. Chi, S. H. Liu, Oxidized divinyl oligoacene-bridged diruthenium complexes: Bridged localized radical characters and reduced aromaticity in bridge cores. *Dalton Trans.* **49**, 16877–16886 (2020).
58. W. Fudickar, T. Linker, Why triple bonds protect acenes from oxidation and decomposition. *J. Am. Chem. Soc.* **134**, 15071–15082 (2012).
59. J. Zhu, K. Zhong, Y. Liang, Z. Wang, T. Chen, L. Y. Jin, Synthesis and self-assembly of oligomers containing cruciform 9,10-bis(arylethynyl)anthracene unit: Formation of supramolecular nanostructures based on rod-length-dependent organization. *Tetrahedron* **70**, 1230–1235 (2014).
60. V. S. Barlier, C. W. Schlenker, S. W. Chin, M. E. Thompson, Acetylide-bridged tetracene dimers. *Chem. Commun.* **47**, 3754–3756 (2011).
61. T. Iwanaga, Y. Yamamoto, K. Nishioka, S. Toyota, Efficient synthesis and electronic spectra of unsymmetrical 5,12-diethynyltetracene derivatives. *Synthesis* **47**, 3997–4007 (2015).
62. M. Lijina, A. Benny, R. Ramakrishnan, N. G. Nair, M. Hariharan, Exciton isolation in cross-pentacene architecture. *J. Am. Chem. Soc.* **142**, 17393–17402 (2020).
63. Z. Wei, Z.-Y. Gu, R. K. Arvapally, Y.-P. Chen, R. N. McDougald Jr., J. F. Ivy, A. A. Yakovenko, D. Feng, M. A. Omary, H.-C. Zhou, Rigidifying fluorescent linkers by metal–organic framework formation for fluorescence blue shift and quantum yield enhancement. *J. Am. Chem. Soc.* **136**, 8269–8276 (2014).
64. C. Healy, K. M. Patil, B. H. Wilson, L. Hermanspahn, T. D. Bennett, The thermal stability of metal-organic frameworks. *Coord. Chem. Rev.* **419**, 213388 (2020).
65. A. D. Wiersum, E. Soubeyrand-Lenoir, Q. Yang, B. Moulin, V. Guillerm, M. B. Yahia, S. Bourrelly, A. Vimont, S. Miller, C. Vagner, An evaluation of UiO-66 for gas-based applications. *Chem. Aisan J.* **6**, 3270–3280 (2011).
66. C. Zhang, L. Xin, J. Li, J. Cao, Y. Sun, X. Wang, J. Luo, Y. Zeng, Q. Li, Y. Zhang, Metal–organic framework (MOF)-based ultrasound-responsive dual-sonosensitizer nanoplatform for hypoxic cancer therapy. *Adv. Healthc. Mater.* **11**, e2101946 (2022).
67. Y. Zhao, Y. Liu, J. Cao, H. Wang, M. Shao, H. Huang, Y. Liu, Z. Kang, Efficient production of H_2O_2 via two-channel pathway over ZIF-8/C_3N_4 composite photocatalyst without any sacrificial agent. *Appl. Catal. Environ.* **278**, 119289 (2020).
68. Q. Wu, Y. Liu, J. Cao, Y. Sun, F. Liao, Y. Liu, H. Huang, M. Shao, Z. Kang, A function-switchable metal-free photocatalyst for the efficient and selective production of hydrogen and hydrogen peroxide. *J. Mater. Chem. A* **8**, 11773–11780 (2020).
69. E. M. Hol, M. Pekny, Glial fibrillary acidic protein (GFAP) and the astrocyte intermediate filament system in diseases of the central nervous system. *Curr. Opin. Cell Biol.* **32**, 121–130 (2015).
70. D. Zhu, H. Yan, X. Liu, J. Xiang, Z. Zhou, J. Tang, X. Liu, Y. Shen, Intracellularly disintegratable polysulfoniums for efficient gene delivery. *Adv. Funct. Mater.* **27**, 1606826 (2017).
71. C. E. Stout, J. L. Costantin, C. C. Naus, A. C. Charles, Intercellular calcium signaling in astrocytes via ATP release through connexin hemichannels. *J. Biol. Chem.* **277**, 10482–10488 (2002).
72. P. Dias, T. Desplantez, M. A. El-Harasis, R. A. Chowdhury, N. D. Ullrich, A. Cabestrero de Diego, N. S. Peters, N. J. Severs, K. T. MacLeod, E. Dupont, Characterisation of connexin expression and electrophysiological properties in stable clones of the HL-1 myocyte cell line. *PLOS ONE* **9**, e90266 (2014).
73. Q. A. Le, J.-C. Kim, K.-H. Kim, A. T. Van Vu, S.-H. Woo, Distinct shear-induced Ca^{2+} signaling in the left and right atrial myocytes: Role of P2 receptor context. *J. Mol. Cell. Cardiol.* **143**, 38–50 (2020).
74. N. Wang, E. De Vuyst, R. Ponsaerts, K. Boengler, N. Palacios-Prado, J. Wauman, C. P. Lai, M. De Bock, E. Decrock, M. Bol, Selective inhibition of Cx43 hemichannels by Gap19 and its impact on myocardial ischemia/reperfusion injury. *Basic Res. Cardiol.* **108**, 1–16 (2013).
75. M. Goldberg, M. De Pittà, V. Volman, H. Berry, E. Ben-Jacob, Nonlinear gap junctions enable long-distance propagation of pulsating calcium waves in astrocyte networks. *PLOS Comput. Biol.* **6**, e1000909 (2010).
76. G. V. Orsinger, J. D. Williams, M. Romanowski, Focal activation of cells by plasmon resonance assisted optical injection of signaling molecules. *ACS Nano* **8**, 6151–6162 (2014).
77. R. Ronan, A. Kshirsagar, A. L. c. Rebelo, A. Sunny, M. Kilcoyne, R. O. Flaherty, P. M. Rudd, G. Schlosser, R. Saldova, A. Pandit, Distinct glycosylation responses to spinal cord injury in regenerative and nonregenerative models. *J. Proteome Res.* **21**, 1449–1466 (2022).
78. H. Ruan, J. Gao, X. Qi, Y. Tao, X. Guo, Z. Guo, L. Zheng, Y. Song, Y. Liao, W. Shen, Visual experience dependent regulation of neuronal structure and function by histone deacetylase 1 in developing Xenopus tectum in vivo. *Dev. Neurobiol.* **77**, 947–962 (2017).
79. W. Shen, H.-H. Liu, L. Schiapparelli, D. McClatchy, H.-y. He, J. R. Yates, H. T. Cline, Acute synthesis of CPEB is required for plasticity of visual avoidance behavior in Xenopus. *Cell Rep.* **6**, 737–747 (2014).
80. A. Ø. Tjell, K. Almdal, Diffusion rate of hydrogen peroxide through water-swelled polyurethane membranes. *Sens. Bio-Sens. Res.* **21**, 35–39 (2018).
81. G. W. T. M. J. Frisch, H. B. Schlegel, G. E. Scuseria, M. A. Robb, J. R. Cheeseman, G. Scalmani, V. Barone, B. Mennucci, G. A. Petersson, H. Nakatsuji, M. Caricato, X. Li, H. P. Hratchian, A. F. Izmaylov, J. Bloino, G. Zheng, J. L. Sonnenberg, M. Hada, M. Ehara, K. Toyota, R. Fukuda, J. Hasegawa, M. Ishida, T. Nakajima, Y. Honda, O. Kitao, H. Nakai, T. Vreven, J. A. Montgomery, J. J. E. Peralta, F. Ogliaro, M. Bearpark, J. J. Heyd, E. Brothers, K. N. Kudin, V. N. Taroverov, T. Keith, R. Kobayashi, J. Normand, K. Raghavachari, A. Rendell, J. C. Burant, S. S. Iyengar, J. Tomasi, M. Cossi, N. Rega, J. M. Millam, M. Klene, J. E. Knox, J. B. Cross, V. Bakken, C. Adamo, J. Jaramillo, R. Gomperts, R.E. Stratmann, O. Yazyev, A. J. Austin, R. Cammi, C. Pomelli, J. W. Ochterski, R. L. Martin, K. Morokuma, V. G. Zakrzewski, G. A. Voth, P. Salvador, J. J. Dannenberg, S. Dapprich, A. D. Daniels, O. Farkas, J. B. Foresman, J. V. Ortiz, J. Cioslowski, D. J. Fox, *Gaussian 09 (Revision D.01)* (Gaussian, 2013).
82. R. Krishnan, J. S. Binkley, R. Seeger, J. A. Pople, Self-consistent molecular orbital methods. XX. A basis set for correlated wave functions. *J. Chem. Phys.* **72**, 650–654 (1980).
83. F. Weigend, R. Ahlrichs, Balanced basis sets of split valence, triple zeta valence and quadruple zeta valence quality for H to Rn: Design and assessment of accuracy. *Phys. Chem. Chem. Phys.* **7**, 3297–3305 (2005).
84. S. Xu, T. He, J. Li, Z. Huang, C. Hu, Enantioselective synthesis of D-lactic acid via chemocatalysis using MgO: Experimental and molecular-based rationalization of the triose's reactivity and preliminary insights with raw biomass. *Appl. Catal. Environ.* **292**, 120145 (2021).
85. S. Grimme, J. Antony, S. Ehrlich, H. Krieg, A consistent and accurate ab initio parametrization of density functional dispersion correction (DFT-D) for the 94 elements H-Pu. *J. Chem. Phys.* **132**, 154104 (2010).
86. C. Gonzalez, H. B. Schlegel, An improved algorithm for reaction path following. *J. Chem. Phys.* **90**, 2154–2161 (1989).

Acknowledgments: We thank Y. Zhao for offering us IIId and IIIe. We thank M. Jiang for help with ESR measurements. We acknowledge support from L. Chen in cyclic voltammetry measurement. We thank Y. Hu for the 3D diffusion calculation. **Funding:** This work received support from the National Key R&D Program of China (no. 2020YFA0908503), the National Natural Sciences Foundation of China (nos. 22105055, 31871041, and 22161142015), the Natural Science Foundation of Zhejiang Province (no. LQ22E03001), the Natural Science Foundation of Hebei Province (no. F2021203102), the Scientific Research Start-up Foundation of Hangzhou Normal University (nos. 2021QDL015 and 2019QDL026), and the Hangzhou Leading Innovation and Entrepreneurship Team Project (TD2022001). **Author contributions:** J.L., D.Z., and W.S. conceived and supervised the project. D.Z., Z.Z., and Y.M. performed the synthesis, material characterizations, and cell experiment. Y.L. and Z.Z. performed the animal experiment. D.Z. performed the data analysis and calculation. All authors have given approval to the final version of the manuscript. **Competing interests:** The authors declare that they have no competing interests. **Data and materials availability:** All data needed to evaluate the conclusions in the paper are present in the paper and/or the Supplementary Materials.

Submitted 25 September 2023
Accepted 18 March 2024
Published 19 April 2024
10.1126/sciadv.adl0263